

PIK Report

No. 72

WAVELETS BASED
ON LEGENDRE POLYNOMIALS

Jochen Fröhlich & Markus Uhlmann



POTSDAM INSTITUTE
FOR
CLIMATE IMPACT RESEARCH (PIK)

Authors:

Dr. Markus Uhlmann*
Potsdam Institute for Climate Impact Research
P.O. Box 60 12 03, D-14412 Potsdam, Germany
Phone: +49-331-288-2687
Fax: +49-331-288-2695
E-mail: Markus.Uhlmann@pik-potsdam.de
*(corresponding author)

Dr.-Ing. Jochen Fröhlich
Institute for Hydromechanics, University of Karlsruhe
D-76128 Karlsruhe
E-mail: froehlich@ifh.uni-karlsruhe.de

Herausgeber:

Dr. F.-W. Gerstengarbe

Technische Ausführung:

U. Werner

POTSDAM-INSTITUT
FÜR KLIMAOLGENFORSCHUNG
Telegrafenberg
Postfach 60 12 03, 14412 Potsdam
GERMANY
Tel.: +49 (331) 288-2500
Fax: +49 (331) 288-2600
E-mail-Adresse:pik@pik-potsdam.de

POTSDAM, JULI 2001

Abstract

We construct an orthogonal wavelet basis for the interval using a linear combination of Legendre polynomial functions. The coefficients are taken as appropriate roots of Chebyshev polynomials of the second kind, as has been proposed in reference [1]. A multi-resolution analysis is implemented and illustrated with analytical data and real-life signals from turbulent flow fields.

1 Introduction

Fischer and Prestin [1] have shown a general method for constructing wavelet bases on the interval based upon orthogonal polynomials. The only example—amongst those cited in the above reference—in which the basis has the orthogonality property, is built from Chebyshev functions of the second kind, which leads to a scalar product weighted by the function $w(x) = (1 - x^2)^{1/2}$. For the purpose of data analysis, any weight other than unity is undesirable since the interpretation of coefficient values w.r.t. their energy contributions turns out to be non-intuitive. Prestin (private communication) proposed a modification to the original construction in which a “hybrid” basis would be built from Chebyshev and Legendre polynomials, thereby carrying over the orthogonality of the original Chebyshev-only basis to a weight function of unity.

In [1] linear combinations of orthogonal polynomials $P_k(x)$ are used for constructing scaling functions $\varphi_{ji}(x)$ and wavelet functions $\psi_{ji}(x)$, where j is the scale index and i the translational (position) index. The former functions (φ) are assembled from low-order polynomials, while the latter (ψ) re-group higher-order-only contributions, viz.

$$\varphi_{ji}(x) = \sum_{k=0}^{2^j} a_{ijk} P_k(x), \quad (1a)$$

$$\psi_{ji}(x) = \sum_{k=2^j+1}^{2^{j+1}} b_{ijk} P_k(x). \quad (1b)$$

The construction can be applied to general orthogonal polynomials. Here, we consider the case of the interval $[-1, 1]$ and define a scalar product with respect to a given weight function $w(x)$ as $\langle f(x), g(x) \rangle_w = \int_{-1}^1 f(x)g(x)w(x)dx$. For wavelets and scaling functions spanning an orthonormal basis of a multi-resolution analysis (MRA), these need to fulfill the following orthogonality conditions:

$$\langle \varphi_{ji}, \varphi_{jl} \rangle_w = \delta_{il}, \quad (2a)$$

$$\langle \psi_{ji}, \psi_{ml} \rangle_w = \delta_{il} \delta_{jm}, \quad (2b)$$

$$\langle \varphi_{ji}, \psi_{ml} \rangle_w = 0, \quad (m \geq j). \quad (2c)$$

Substituting the ansatz (1), we obtain:

$$\langle \varphi_{ji}, \varphi_{jl} \rangle_w = \sum_{k=0}^{2^j} \sum_{n=0}^{2^j} a_{ijk} a_{lnm} \langle P_k, P_n \rangle_w, \quad (3a)$$

$$\langle \psi_{ji}, \psi_{ml} \rangle_w = \sum_{k=2^j+1}^{2^{j+1}} \sum_{n=2^m+1}^{2^{m+1}} b_{ijk} b_{lnm} \langle P_k, P_n \rangle_w, \quad (3b)$$

$$\langle \varphi_{ji}, \psi_{ml} \rangle_w = \sum_{k=0}^{2^j} \sum_{n=2^m+1}^{2^{m+1}} a_{ijk} b_{lnm} \langle P_k, P_n \rangle_w. \quad (3c)$$

It is clear that due to the orthogonality of the polynomials (i.e. $\langle P_k, P_n \rangle_w = \delta_{kn}$) the choice of the

coefficients a, b alone determines the orthogonality properties of the basis. Therefore, we find:

$$\langle \varphi_{ji}, \varphi_{jl} \rangle_w = \sum_{k=0}^{2^j} a_{ijk} a_{ljk}, \quad (4a)$$

$$\langle \psi_{ji}, \psi_{ml} \rangle_w = \delta_{jm} \sum_{k=2^j+1}^{2^{j+1}} b_{ijk} b_{ljk}, \quad (4b)$$

$$\langle \varphi_{ji}, \psi_{ml} \rangle_w = 0, \quad (m \geq j). \quad (4c)$$

The factor δ_{jm} in relation (4b) follows from the fact that the bounds of the two sums in (3b) need to be equal if the scalar product is to be non-zero.

As a consequence it is possible to interchange freely the particular type of polynomial—amongst the class of orthogonal ones—without changing the above properties. Therefore, we can go about and modify a given basis whose a 's and b 's are such that (2) is verified and replace its $P_k(x)$'s with Legendre polynomials which have an associated weight $w(x) = 1$. In the following we will take a closer look at these Legendre wavelets.

2 The wavelet basis

2.1 Definition

We define the following wavelets and scaling functions based upon Legendre polynomials $L_k(x)$ and coefficients related to the Chebyshev polynomials of the second kind $U_k(x)$:

$$\varphi_{ji}(x) = C_{ij}^\varphi \cdot \sum_{k=0}^{2^j} U_k(y_i^{(2^j+1)}) \cdot \sqrt{k+1/2} \cdot L_k(x), \quad j = 0, 1, \dots, i = 0 \dots 2^j \quad (5a)$$

$$\psi_{ji}(x) = C_{ij}^\psi \cdot \sum_{k=2^j+1}^{2^{j+1}} U_k(y_i^{(2^j)}) \cdot \sqrt{k+1/2} \cdot L_k(x), \quad j = 0, 1, \dots, i = 0 \dots 2^j - 1 \quad (5b)$$

where $L_k(x)$ and $U_k(x)$ on the interval $x \in [-1, 1]$ can be defined by [2]

$$L_k(x) = \frac{1}{2^k} \sum_{l=0}^{\text{int}(k/2)} (-1)^l \binom{k}{l} \binom{2k-2l}{k} x^{k-2l}, \quad (6a)$$

$$U_k(x) = \frac{\sin((k+1) \arccos(x))}{\sin(\arccos(x))}, \quad (6b)$$

or in terms of their three-point recursion formula

$$L_{k+1}(x) = \frac{2k+1}{k+1} x L_k(x) - \frac{k}{k+1} L_{k-1}(x), \quad L_0(x) = 1, \quad L_1(x) = x, \quad (7a)$$

$$U_{k+1}(x) = 2x U_k(x) - U_{k-1}(x), \quad U_0(x) = 1, \quad U_1(x) = 2x. \quad (7b)$$

The parameters $y_i^{(n)}$ in equations (5) are the zeroes of the n th order Chebyshev polynomial of the second kind, i.e.

$$y_i^{(n)} = -\cos\left(\frac{(i+1)\pi}{n+1}\right), \quad i = 0 \dots n-1. \quad (8)$$

For convenience, the present numbering is different from the standard numbering in that we have $y_i^{(n)} < y_{i+1}^{(n)}$. Equations (5) define the coefficients a_{ijk} and b_{ijk} in (1). In [1] the orthogonality of the resulting basis with $P_k = U_k$ in (1) is proved. As discussed above, this property carries over to the functions defined by (5). The constant factors $C_{ij}^\varphi, C_{ij}^\psi$ are introduced for the purpose of normalization in order to fulfill equations (2) without further constants. We obtain

$$C_{ij}^\varphi = \left[\sum_{k=0}^{2^j} \left(\frac{\sin [(k+1)(i+1)\pi/(2^j+2)]}{\sin [(i+1)\pi/(2^j+2)]} \right)^2 \right]^{-1/2}, \quad (9a)$$

$$C_{ij}^\psi = \left[\sum_{k=2^j+1}^{2^{j+1}} \left(\frac{\sin [(k+1)(i+1)\pi/(2^j+1)]}{\sin [(i+1)\pi/(2^j+1)]} \right)^2 \right]^{-1/2}. \quad (9b)$$

With the above functions φ, ψ , the following decomposition of a square-integrable function $u(x)$ is possible

$$u(x) = c_{00} \varphi_{00}(x) + c_{01} \varphi_{01}(x) + \sum_{j=0}^{\infty} \sum_{i=0}^{2^j-1} d_{ji} \psi_{ji}(x), \quad (10)$$

where, by orthonormality, the coefficients are obtained from

$$d_{ji} = \int_{-1}^1 u(x) \psi_{ji}(x) dx, \quad (11a)$$

$$c_{ji} = \int_{-1}^1 u(x) \varphi_{ji}(x) dx. \quad (11b)$$

Again due to orthonormality the decomposition (10) yields a corresponding decomposition of the “energy” of the signal in terms of the coefficients

$$\int_{-1}^1 u(x)^2 dx = c_{00}^2 + c_{01}^2 + \sum_{j,i} d_{ji}^2. \quad (12)$$

2.2 Convergence of the approximation

We illustrate the global convergence of the approximation of a function by its wavelet expansion through numerical tests with analytical signals. For that purpose, a partial reconstruction according to equation (10) with the upper bound of the j -summation being $J < \infty$ is performed. As a representative example, Figure 8 shows the variation of the maximum error and the L_2 -error for the signal $u(x) = \exp(-4x^2)$ when the truncation index J is increased. Spectral convergence is observed. This is to be expected, and in fact constituted a test for the implementation, since the truncated wavelet sum by means of (5) is just a re-ordered Legendre expansion. Hence, the approximating function is the same in both cases resulting in the same convergence behavior.

At present, the scalar products (11) are evaluated by a Gauss-Lobatto quadrature, i.e. first performing a Legendre transform of the data—sampled on a Gauss-Lobatto grid—and then computing the linear combination of Legendre coefficients which leads to the respective wavelet coefficients. If data is given in terms of coefficients of orthogonal polynomials of a different type, explicit conversion formulas can be used [e.g 3] or spectral interpolation onto the Legendre grid might be considered (cf. § 2.6). The construction of a fast version of the present algorithm is left as a future extension.

Legendre wavelets			Chebyshev wavelets		
j	i	x_{tail}	$\int_{x_{tail}}^{+1} \psi_{ji}^2 dx$	x_{tail}	$\int_{x_{tail}}^{+1} \psi_{ji}^2 dx$
5	15	0.879	6.17e-3	0.933	4.40e-2
	12	0.850	1.46e-2	0.933	1.17e-1
	10	0.922	1.67e-2	0.933	1.59e-1
	8	0.922	2.80e-2	0.962	2.03e-1
	6	0.922	5.54e-2	0.996	2.15e-1
	4	0.957	7.87e-2	0.996	3.31e-1
7	63	0.844	1.79e-3	0.953	1.12e-2
	50	0.932	2.15e-3	0.992	2.29e-2
	40	0.932	3.79e-3	0.992	3.47e-2
	30	0.932	7.64e-3	0.992	5.29e-2
	20	0.975	1.04e-2	0.992	8.66e-1

Table 1: Energy contained in the “tails” of the wavelet functions at two different levels j and various positions i (cf. Figure 2 and 3). The “tail-location” x_{tail} has been determined visually, using a grid with $N = 1024$, and the integral has been evaluated by a low-order quadrature. For comparison, the last two columns show the corresponding quantities computed for the wavelets of Fischer and Prestin [1] based upon Chebyshev polynomials of the second kind.

2.3 Localization properties

Figure 1 shows some wavelet functions of scale $j = 5$. It can be observed that they are close to being translationally invariant near the center of the interval, while they visibly increase their amplitude and frequency near the boundary. This effect of varying shape is more vividly illustrated in Figure 2, where the “envelope” of the square of several wavelet functions is shown. Particularly, the existence of a second local maximum of the amplitude at the nearest boundary can be observed. From the semi-logarithmical plots in Figure 3 the spatial decay of the functions around their center location can be judged. This decay is approximately $\mathcal{O}(x^{-2})$ (cf. Figure 5), i.e. the wavelets themselves decay at a rate of $1/x$.

The decay, however, is only local while close to the boundaries the wavelet functions have a tendency to increase and to exhibit the “tails” mentioned above. Table 1 gives the contribution of these “tails” to the energy of the wavelet, i.e. the integral $\int_{x_{tail}}^{+1} \psi_{ji}^2 dx$ with x_{tail} being the—visually determined—location where the slope of the envelope reverses. This quantity is below one percent for centrally located wavelets.

For comparison, Figure 4 shows the corresponding decay of the wavelets of Fischer and Prestin [1] which are based upon Chebyshev polynomials of the second kind (U_k instead of L_k in (5)). In the latter case the “tails” are similar and even more pronounced. This is also reflected in the values of Table 1.

We recall that both families of wavelets are related through the basic equation (1) inasmuch as they have common coefficients a_{ijk}, b_{ijk} and only differ in the definition of the associated polynomial function $P_k(x)$. These coefficients a_{ijk} are plotted in Figure 6 where the same indices i, j as in the graphs discussing the decay have been chosen. At the same time, the coefficients represent the Legen-

dre spectrum of the present wavelets. It is evident from the graphs that the exact spectral distribution of the basis functions varies with the position index. However, the low-pass filter nature of the scaling functions and the band-pass property of the wavelets is obvious.

One question which arises naturally with respect to the usefulness of the current basis is its ability to pick up existing features of a given signal without creating artifacts due to the particular shape of the wavelet functions near the boundary. We will address this point in § 2.5.

2.4 Definition of a scale parameter

From the definition of the wavelets and from the plots in Figure 1 it is obvious that the period of oscillation of wavelets with the same scale index j varies over the interval. Hence, the physical “scale” is no more constant with the scale index j but changes with the position index i . Defining a “scale” and drawing a scalogram hence becomes a delicate issue. Here we use the centers of the wavelet functions for this purpose as described now.

Recall that the zeroes of the Legendre polynomials are not available in closed form. As a consequence, the locations of the “centers” of the wavelets and scaling functions defined here are not available in closed form but need to be determined numerically. To be specific, by “centers” $z_{ji}^\varphi, z_{ji}^\psi$ we mean the position of the largest positive local maximum values, excluding the boundaries of the interval, which can be obtained e.g. by a fixed point iteration of the first derivative of (5). In practice, this procedure is however very cumbersome and an analytic expression—even approximate—would be preferable, particularly in view of the way of presenting information with respect to scale as discussed below. Therefore, we propose—solely for the definition of the “scale” of a wavelet function—to work with the roots of the Chebyshev polynomials of the second kind instead and define:

$$\hat{z}_{ji}^\varphi = y_i^{(2^j+1)}, \quad (13a)$$

$$\hat{z}_{ji}^\psi = y_i^{(2^j)}, \quad (13b)$$

with y given in (8). Figure 7 shows the difference between the two definitions z_{ji}^ψ and \hat{z}_{ji}^ψ . It exhibits a minimum in the center of the interval and near the boundaries.

For the purpose of data analysis, we will associate a physical scale parameter to each wavelet function. In the classical MRA, where wavelets are translationally invariant, the scale is simply $s_j = 2^{-j}L_x$, where L_x is the physical size of the domain. We solve this problem by defining the discrete scale parameter s_{ji} as follows

$$s_{ji} = \frac{L_x}{2} \begin{cases} \frac{z_{ji+1}^\psi + z_{ji}^\psi}{2} + 1 & \text{if } i = 0 \\ 1 - \frac{z_{ji}^\psi + z_{ji-1}^\psi}{2} & \text{if } i = 2^j - 1 \\ \frac{z_{ji+1}^\psi - z_{ji-1}^\psi}{2} & \text{else} \end{cases} \quad (14)$$

This results from a division of the interval into subintervals according to the mid-points between neighboring center locations. Consequently, it implies that $\sum_i s_{ji} = L_x$ and in particular that $s_{00} = L_x$. Unfortunately, the quantity s_{ji} can not be determined analytically if the exact centers z_{ji}^ψ are used. As a remedy we propose to use the roots of the Chebyshev polynomials \hat{z}_{ji}^ψ in (14) which upon

substitution of (8) leads to

$$s_{ji}(\hat{z}_{ji}^\psi) = \frac{L_x}{2} \begin{cases} \cos\left(\frac{(2^j - 1/2)\pi}{2^j + 1}\right) \cos\left(\frac{\pi/2}{2^j + 1}\right) + 1 & \text{if } i = 0 \\ 1 - \cos\left(\frac{3/2\pi}{2^j + 1}\right) \cos\left(\frac{\pi/2}{2^j + 1}\right) & \text{if } i = 2^j - 1 \\ \sin\left(\frac{(i+1)\pi}{2^j + 1}\right) \sin\left(\frac{\pi}{2^j + 1}\right) & \text{else} \end{cases} \quad (15)$$

Figure 7 shows the resulting relative difference in scale between the definition of s_{ji} with the exact and with the approximated centers. These differences are only appreciable near the boundary, where they amount to a very localized maximum of 25 percent. In the present situation, the definition of a “scale” associated to a wavelet certainly is somewhat arbitrary, in particular close to the boundaries. We therefore feel that the definition (15) suits the purpose of data analysis and visualization.

Two ways of presenting the coefficients of the present transform can be constructed based on the above definitions of the scale parameter s_{ji} . They will be detailed and illustrated by means of analytical signals in the following paragraph. In the sequel, we will then adopt the definition (15).

2.5 Transform of analytical signals and coefficient scheme

Before considering real-life signals it is instructive to study the transform itself by means of analytical signals. We consider as a first case the transform of a periodic signal, $u(x) = \sin(2\pi x a)$, with various frequencies a . This is a particular case of a signal which can be analyzed with the present new algorithm as well as with a standard method for periodic signals.

Let us now discuss the way of visually presenting the resulting coefficients. In Figures 9 and 10 we confront two different types of drawing scalograms from the same coefficient values. In the first method (Figure 10), the “exact”—i.e. iteratively determined—center locations \hat{z}_{ji}^ψ and resulting scales $s_{ji}(z_{ji})$ are used to define rectangular cells Ω_{ji} in the following way:

- (a1) The center of Ω_{ji} is defined by the coordinate pair $(\hat{z}_{ji}^\psi, -\log_2(s_{ji}))$.
- (a2) The width of Ω_{ji} is equal to the scale s_{ji} .
- (a3) The height of Ω_{ji} is set to an arbitrary constant value.

The plot is then obtained by drawing each cell colored with the absolute value of the corresponding wavelet coefficient. Note that due to some overlapping of the rectangles they seem to have the shape of more irregular polygons.

The other type of visual presentation—method (b)—in Figure 9 has been obtained by using the approximate definition of center points and scales via the roots of the Chebyshev polynomials of the second kind. Introducing the parameter $\theta_{ji} = \pi(i+1)/(2^j + 1)$, we can rewrite the definitions (13), (15) as

$$\hat{z}_{ji}^\psi = \cos(\theta_{ji}), \quad (16a)$$

$$s_{ji}(\hat{z}_{ji}^\psi) = -\frac{L_x}{2} \sin(\theta_{ji}) \sin\left(\frac{\pi}{2^j + 1}\right) \quad 0 < i < 2^j - 1, \quad (16b)$$

The previous relations represent a discrete mapping from dyadic θ_{ji} to \hat{z}_{ji} and s_{ji} , respectively, which we can extend to the continuous case by replacing θ_{ji} with $\theta \in]0, \pi[$. In this fashion, we can construct a scalogram with cell boundaries which are progressively deformed such as to indicate a spatial change of scale at fixed scale index j . In practice, we proceed as follows:

- (b1) Define a classical scalogram with rectangular cells centered at $(\theta_{ji}, -\log_2(s_{ji}(\hat{z}_{j,i=2^j/2})))$, i.e. using the scale of the centrally located wavelets given in (15), and separate the cells at the mid-points between neighbors.
- (b2) Transform the coordinate locations of the cell boundaries by the maps $x = \cos(\theta)$, $y = -\log_2(\sin(\theta))$.

The result is a pattern with strips of coefficients of common scale index j which are bent upwards near the boundaries. By this method the coefficient values corresponding to small scale indices j appear at different physical scales along their horizontal extent which in a way is a visual representation of the fact that a single wavelet undergoes a similar variation in frequency along the interval. As Figures 9 and 10 demonstrate, both methods of visualization are of fairly similar quality with respect to the readability of frequency content and position of the signal. For its smoothness and, because it allows for a natural partitioning of the ordinate without gaps, we will henceforth retain method (b).

It can be seen in Figure 9 that the present base correctly shows a response at approximately constant scale across the interval. Observe that the use of a real-valued wavelet always tends to yield small-scale oscillations of the coefficients due to cancellations between the signal and the wavelet itself. Therefore, a pure sine wave does not show up as a solid line in the scalogram, but rather as a horizontal band with alternating values.

Next, let us turn to the transform of a Gaussian bump, $u(x) = \exp(-((x - x_c)/(2\sigma))^2)$, with different standard deviations σ and center locations x_c . Here, the question is whether the position of the peak can be correctly determined from the scalogram and if information on the characteristic scale can be extracted in this fashion. Looking at Figures 11–12, both seems to be the case. The maximum amplitudes of the coefficients are not exactly pyramid-shaped when x_c is off-center, but they do approximately point to the x_c -locations. Furthermore, the scale of the cusp (i.e. the smallest scale where a large amplitude is recorded) corresponds to the scale of the signal. The observed difference between the cusps of the scalograms in Figure 11 and 12 is of roughly two octaves, i.e. a factor of 4, while the standard deviation of the data varies fivefold.

2.6 Transform of data from turbulent flow and wavelet spectra

Figure 13 shows the transform of signals from a turbulent plane channel flow simulation of the second author. The flow is fully developed and has a friction-velocity-based Reynolds number of $Re_\tau = 590$ and is therefore similar to the highest Reynolds number case studied in [4], except that the spatial resolution has been increased substantially. The present data represents instantaneous wall-normal profiles of the three velocity fluctuation components which have been spectrally interpolated from 385 Chebyshev modes to a $N = 256$ Legendre-Gauss-Lobatto grid. In turbulent channel flow, high gradients and small structures are generated close to the solid surfaces, i.e. at the extrema of our interval. In this particular snapshot, the streamwise component u' shows such features near $x = -1$ and $x = 1$, both of which are not unlike the narrow Gaussian bumps of § 2.5. The wavelet coefficient scalogram again allows a localization of these peaks as well as a reading of their relative scales. Several coarser undulations of u' towards the center of the interval provoke responses at larger scales.

We are now in a position to quantify these arguments somewhat more by looking at energy spectra from the proposed wavelet analysis. Let us first define a *global* power-spectral density per unit wavenumber as follows:

$$E(k_m) = \frac{1}{\Delta k_m} \sum_{j,i / k_L^m \leq k_{ji} \leq k_R^m} d_{ji}^2 . \quad (17)$$

As indicated, the index pairs (i, j) are selected such that the resulting “wavenumber”, i.e. inverse scale $k_{ji} = 1/s_{ji}$, falls into one of a total number of M pre-determined bins $[k_L^m, k_R^m]$, where $1 \leq m \leq M$. The function (17) is normalized by the wavenumber increment Δk_m in order for the following equality to hold for the total energy:

$$E_{tot} = \int_{-1}^{+1} u(x)^2 dx = \sum_{i=0}^1 c_{0i}^2 + \sum_{j=0}^J \sum_{i=0}^{2^j-1} d_{ji}^2 = \sum_{i=0}^1 c_{0i}^2 + \sum_{m=1}^M E(k_m) \Delta k_m . \quad (18)$$

In the following, the bins are spaced logarithmically.

Next, we define a *local* power-spectral density per unit wavenumber:

$$E(k_j, x) = \frac{d_{j,i_c}^2}{\Delta k_j} , \quad (19)$$

where the position index $i_c = i_c(x)$ corresponds to the wavelet at scale index j whose center $y_{i_c}^{(2^j)}$ lies closest to the location x . In other words, the function $E(k_j, x)$ represents a cut through the scalogram at the abscissa x . Therefore, there are exactly $J+1$ such spectral values at each location and the largest scales are obviously redundantly reproduced in spectra evaluated at small distances from each other. In particular, the $j = 0$ -coefficient will enter all local spectra. In contrast to the fixed wavenumber increment Δk_m in (17), the increment Δk_j is based on $k_{j,i_c} = 1/s_{j,i_c}$, i.e. on the scale parameters of the coefficients actually selected.

Figure 14 shows the local energy spectra of the streamwise velocity data from Figure 13, evaluated at different locations. Not surprisingly, close to the center the largest scales dominate the flow, while there is a distinct medium-scale peak at about midway towards the lower wall ($x = -0.6$) and at $x = -0.94$ the maximum energy is recorded for the small scales.

Figure 15 finally shows the global energy spectrum for the three components of velocity of our instantaneous profile from turbulent channel flow. Also shown are the corresponding Legendre coefficient spectra, albeit in a separate graph. All curves are normalized by the respective total component energy E_{tot} and still a comparison is not useful due to the different meaning of “scale” in both cases (the wavenumber associated to a Legendre coefficient is simply defined as $\tilde{k}_m = m/L_x$). Furthermore, the physical significance of summing-up coefficients over the non-homogeneous flow direction seems unclear.

3 Multi-dimensional basis

3.1 Definition

The construction of a wavelet basis in more than one dimension typically proceeds along either one of the following lines [5, p.313]:

- (i) Design of genuinely multi-dimensional wavelet/scaling functions with the desired orthonormality and angular selectivity properties.
- (ii) Performing a tensor product of one-dimensional bases in each coordinate direction, e.g. setting $\psi_{i_x, i_y}^{j_x, j_y}(x, y) = \psi_{i_x}^{j_x}(x) \cdot \psi_{i_y}^{j_y}(y)$. With this procedure the scale indices are “scrambled” and not directionally invariant.
- (iii) Performing a tensor product of one-dimensional MRAs with a “global” scale index and different wavelets for picking up the various directional features.

We choose the method (iii) for our present purposes since it simplifies the interpretation of signals in terms of scale.

Henceforth we wish to analyze two-dimensional flow data which possesses one periodic (x) and one bounded (y) coordinate direction, i.e. we consider the space $L^2(\mathbb{R}/\mathbb{Z} \times [-1, 1])$. Therefore, we propose a hybrid MRA, composed of a periodic wavelet basis as in [6] and the Legendre wavelet basis of § 2. Let us define the two-dimensional scaling functions and the set of three wavelet functions as follows:

$$\varphi_{i_x, i_y}^j(x, y) = \tilde{\varphi}_{j, i_x}(x) \cdot \varphi_{j, i_y}(y) \quad i_y = 0 \dots 2^j \quad (20a)$$

$$\psi_{i_x, i_y}^{j,1}(x, y) = \tilde{\varphi}_{j, i_x}(x) \cdot \psi_{j, i_y}(y) \quad i_y = 0 \dots 2^j - 1 \quad (20b)$$

$$\psi_{i_x, i_y}^{j,2}(x, y) = \tilde{\psi}_{j, i_x}(x) \cdot \varphi_{j, i_y}(y) \quad i_y = 0 \dots 2^j \quad (20c)$$

$$\psi_{i_x, i_y}^{j,3}(x, y) = \tilde{\psi}_{j, i_x}(x) \cdot \psi_{j, i_y}(y) \quad i_y = 0 \dots 2^j - 1 \quad (20d)$$

where in all cases $j = 0, 1, \dots$ and $i_x = 0 \dots 2^j - 1$. The functions $\varphi(y), \psi(y)$ are defined in (5); the periodic functions $\tilde{\varphi}(x), \tilde{\psi}(x)$ are spline wavelets of order 4 and can be found in detail in references [6, 7]. Let us recall that the two-dimensional scaling function φ_{i_x, i_y}^j represents the smooth content of the signal at scale index j while the wavelets $\psi_{i_x, i_y}^{j,1}, \psi_{i_x, i_y}^{j,2}, \psi_{i_x, i_y}^{j,3}$ pick up the detail information with respect to horizontal (x), vertical (y) and diagonal variations of the signal, respectively.

The resulting decomposition of a two-dimensional function is as follows (recall that $J = \log_2(N) - 1$):

$$u(x, y) = c_{0,0}^0 \varphi_{0,0}^0(x, y) + c_{0,1}^0 \varphi_{0,1}^0(x, y) + \sum_{j=0}^J \sum_{i_x=0}^{2^j-1} \left[\sum_{i_y=0}^{2^j} d_{i_x, i_y}^{j,2} \psi_{i_x, i_y}^{j,2}(x, y) + \sum_{q=\{1,3\}} \sum_{i_y=0}^{2^j-1} d_{i_x, i_y}^{j,q} \psi_{i_x, i_y}^{j,q}(x, y) \right], \quad (21)$$

which leads to a total number of $2 + \sum_{j=0}^J \{2^j(2^j + 1) + 2 \cdot 2^{2j}\} = N(N + 1)$ coefficients, as it should. Splitting the sums results from the different number of scaling functions and wavelets with the Legendre construction which is already reflected by the index bounds in (20).

Due to orthogonality the coefficients are obtained from the following scalar products:

$$d_{i_x, i_y}^{j,q} = \int_x \int_y u(x, y) \psi_{i_x, i_y}^{j,q}(x, y) dy dx, \quad (22a)$$

$$c_{i_x, i_y}^j = \int_x \int_y u(x, y) \varphi_{i_x, i_y}^j(x, y) dy dx, \quad (22b)$$

The integrals can be factorized because of the tensorial nature of the wavelets and scaling functions. Therefore, we can first apply the standard Mallat algorithm to each “row” of data at constant y and then proceed by scale-wise computing the remaining integration in the y -direction by our $\mathcal{O}(N^2)$ scheme of § 2.2. The present decomposition algorithm therefore needs $\mathcal{O}(\log(N) N^3)$ operations. As mentioned above, this can be improved with by a recursive algorithm for the non-periodic part.

Figure 16 shows the shape of the three types of wavelets $\psi_{i_x, i_y}^{j,q}(x, y)$, $q = 1, 2, 3$ of the scale index $j = 5$ and at two locations, in the center of the domain and close to the boundary $y = \pm 1$. The localization properties are quite different in the two coordinate directions since spline wavelets have an exponential decay while the Legendre wavelets decay roughly with a power of -1 and exhibit the characteristic “tails” near the boundaries discussed above.

3.2 Transform of a two-dimensional analytical function and the coefficient scheme

When representing the coefficients obtained from a two-dimensional MRA graphically, one customarily uses a block diagram where at each level j the rectangular domain is divided into quarters, three of which are used for representing the current coefficients of level j , $d_{i_x, i_y}^{j,q}(x, y)$, and the fourth one being subdivided again for the following level $j-1$ and so on [8]. We locate the coefficients $d^{j,2}(x, y)$ in the lower left quadrant, $d^{j,3}(x, y)$ in the lower right and $d^{j,1}(x, y)$ in the upper right (cf. the schematic in Figure 17). This arrangement corresponds to the original proposition of Mallat [8] and differs from the one used by Daubechies [5, p.315]. The size of the individual cells which are then color-coded with the absolute values of the wavelet coefficients is set according to our definition of wavelet centers, i.e. uniform in the x -direction and according to the approximate center locations of the Legendre wavelets (13) in the y -direction.

As an analytic test we consider a two-dimensional Gaussian bump now,

$$u(x, y) = \exp\left(-\frac{(x - x_c)^2 + (y - y_c)^2}{(2\sigma)^2}\right) \quad (23)$$

with the finer scale $\sigma = 0.01$ of § 2.5 and three locations, one near the center of the domain, one moderately close to the limit of the interval ($y_c = 0.8$) and one very close to the boundary ($y_c = 0.95$). The domain has been mapped to $\Omega = [0, 2] \times [-1, 1]$ for the analytical tests in this section.

The coefficient diagrams of the transform (Figure 18) demonstrate several points:

- (i) The position of the bump can be correctly determined from the maximum of the response in coefficient space.
- (ii) The intensity of the response in horizontal direction, $q = 1$, does not change between different bump locations, i.e. the maximum response in each scale index remains the same albeit shifted to a new position. This is also approximately true for the diagonal direction $q = 3$.
- (iii) The intensity of the response in the vertical direction $q = 2$ shifts towards smaller scale indices j when the bump is closer to the boundary, e.g. the block $d^{6,2}$ showing a marked response for a centrally located bump is nearly void when $y_c = 0.95$. This reflects the fact that s_{j, i_y} decreases with i_y and is therefore consistent with a constant scale σ of the bump.
- (iv) The response appears much more smeared out in the vertical direction ($d^{j,2}$) than in the two others owing to the relatively poor spatial localization of the Legendre wavelets.

Concerning points (ii)-(iii) we should point to the difficulties of interpreting the present two-dimensional coefficient scheme with respect to scale. The physical scale is not constant within one block of the diagram nor is it isotropic. Rather are we dealing with a horizontal scale $s_x(j) = 2^{-j}$ and a distinct vertical scale $s_y(j, i_y) = s_{j, i_y}$ as defined in (14). In our graphical representation we indicate those scales by choosing rectangular cells for each coefficient, reflecting the two scales by the aspect ratio, i.e. by having flattened cells near the boundaries $y = \pm 1$. Consequently, the same signal—when shifted along the y -coordinate—gradually appears at a different scale index in coefficient space, as has been observed under (iii). However, the present analysis still bears the strict hierarchical feature of the original MRA *locally* in the sense that at a given location the scale varies exponentially with the scale index j .

Finally we present the transform of a signal which consists of Dirac pulses at a set of cross-shaped grid points near the lower boundary of the domain (cf. Figure 19). This test demonstrates the present method's ability to separate directional properties of the signal, i.e. horizontal from vertical

variations. Furthermore, it shows that very sharp gradients produce approximately equally intense responses irrespective of their spatial orientation.

3.3 Transform of a plane from turbulent channel flow data

Figure 20 shows a spanwise/wall-normal plane from the above mentioned turbulent plane channel flow simulation. The size of the domain is $\Omega = [0, \pi] \times [-1, 1]$ which corresponds to 1850×1180 wall units at the chosen Reynolds number. The plotted quantity is a snapshot of the streamwise velocity fluctuations. The original data has a dimension of 600 Fourier modes times 385 Chebyshev modes, which has been spectrally interpolated on a 512 (uniform) by 512 (Legendre-Gauss-Lobatto) grid.

The signal bears a vast number of features and one clearly needs a formalism to help extracting the desired information. Inspecting the wavelet coefficients in Figure 21, the well-known small-scale intermittency [9] is apparent. In the present plot, the greyscales are adapted to vary between $[0, \max_{i_x, i_y, q}(|d_{i_x, i_y}^{j, q}|)]$ for each scale index j and reveal that the high intensity regions become increasingly localized, i.e. less space-filling, with increasing j .

We consistently obtain most high intensity responses from wavelets in block $q = 1$, i.e. corresponding to horizontal variations of the data. This would mean that most of the structures bearing sharp gradients are arranged in a vertical fashion. This observation, however, needs more backing and cross-checking through the analysis of additional snapshots.

4 Conclusion

Starting from [1] we have constructed an orthonormal wavelet basis for the interval by an appropriate recombination of Legendre polynomials. The wavelet functions decay approximately with a power of -1 near their centers and have rising “tails” near the boundaries. Using these ingredients we have implemented a multi-resolution analysis where the scale, however, is now a function of both scale index and position.

The usefulness of the present basis for data analysis is demonstrated by studying the transforms of analytical functions and data from turbulent flow simulations. We have defined local power-spectral density functions and find that they represent an important tool for the analyst.

Note that with the present lumping of blocks of polynomials no better decay than $\propto 1/x$ can be expected. This is readily understood by recalling the similarity with the so-called Shannon wavelets defined by indicator functions in Fourier space. Fourier theory yields a decay of $\propto 1/x$ for discontinuous Fourier transform. With the present construction we are in the same situation. While the rate of decay can not be changed, the actual values and the properties of the “tails” might be improved. Another route is to modify the lumping by using a smoother selection of polynomial coefficients as employed in [10].

In a second part of the paper a hybrid two-dimensional MRA has been proposed and implemented. It is constructed based on the tensor products between a periodic spline wavelets in the first direction and the present Legendre wavelets in the second direction. The implementation of two non-periodic directions can be accomplished in exactly the same way. Higher dimensions are also straightforward.

We have discussed the implications of a spatially varying scale parameter for the graphical representation of the wavelet coefficients defining an appropriate scale parameter for each wavelet. In the two-dimensional case the visualization is performed with an adaption of the coefficient scheme with clustered scale and direction index. The transform of analytical data has again guided the way of interpreting the proposed coefficient scheme, consisting of the usual block-wise presentation combined with individual coefficient “cells” of a size that varies by scale index *and* position.

Finally we have discussed the coefficients obtained by transforming a spanwise plane of turbulent plane channel flow data. The instantaneous velocity fluctuations are found to be more intermittent at small scales than on large scales, an observation which has already become popular in the wavelet community [e.g. 11, p.23].

References

- [1] B. Fischer and J. Prestin. Wavelets based on orthogonal polynomials. *Math. Comp.*, 66(220):1593–1618, 1997.
- [2] M. Abramowitz and I.A. Stegun. *Handbook of mathematical functions*. Dover, 1964.
- [3] R. Askey. *Orthogonal polynomials and special functions*. SIAM, Philadelphia (PA), USA, 1975.
- [4] R.D. Moser, J. Kim, and N.N. Mansour. Direct numerical simulation of turbulent channel flow up to $Re_\tau = 590$. *Phys. Fluids*, 11(4):943–945, 1999.
- [5] I. Daubechies. *Ten lectures on wavelets*. CBMS-NSF Reg. Conf. Series Appl. Math. SIAM, Philadelphia (PA), USA, 1992.
- [6] V. Perrier and C. Basdevant. Periodical wavelet analysis, a tool for inhomogeneous field investigation. Theory and algorithms. *Rech. Aéosp.*, 3:54–67, 1989.
- [7] J. Fröhlich and K. Schneider. An adaptive wavelet Galerkin algorithm for one- and two-dimensional flame computations. *Eur. J. Mech. B/Fluids*, 13(4):439–471, 1994.
- [8] S.G. Mallat. A theory for multiresolution signal decomposition: the wavelet representation. *IEEE Trans. Pattern Analysis Mach. Intell.*, 11(7):674–693, 1989.
- [9] J. Jiménez and A.A. Wray. On the characteristics of vortex filaments in isotropic turbulence. *J. Fluid Mech.*, 373:255–282, 1998.
- [10] R. Grgenson and J. Prestin. Lebesgue constants for an orthogonal polynomial Schauder basis. *Comp. Anal. and Appl.*, 2:159–175, 2000.
- [11] K. Kishida. *Analysis of turbulence in the orthonormal divergence-free wavelet representation*. PhD thesis, Hiroshima University, 2000.

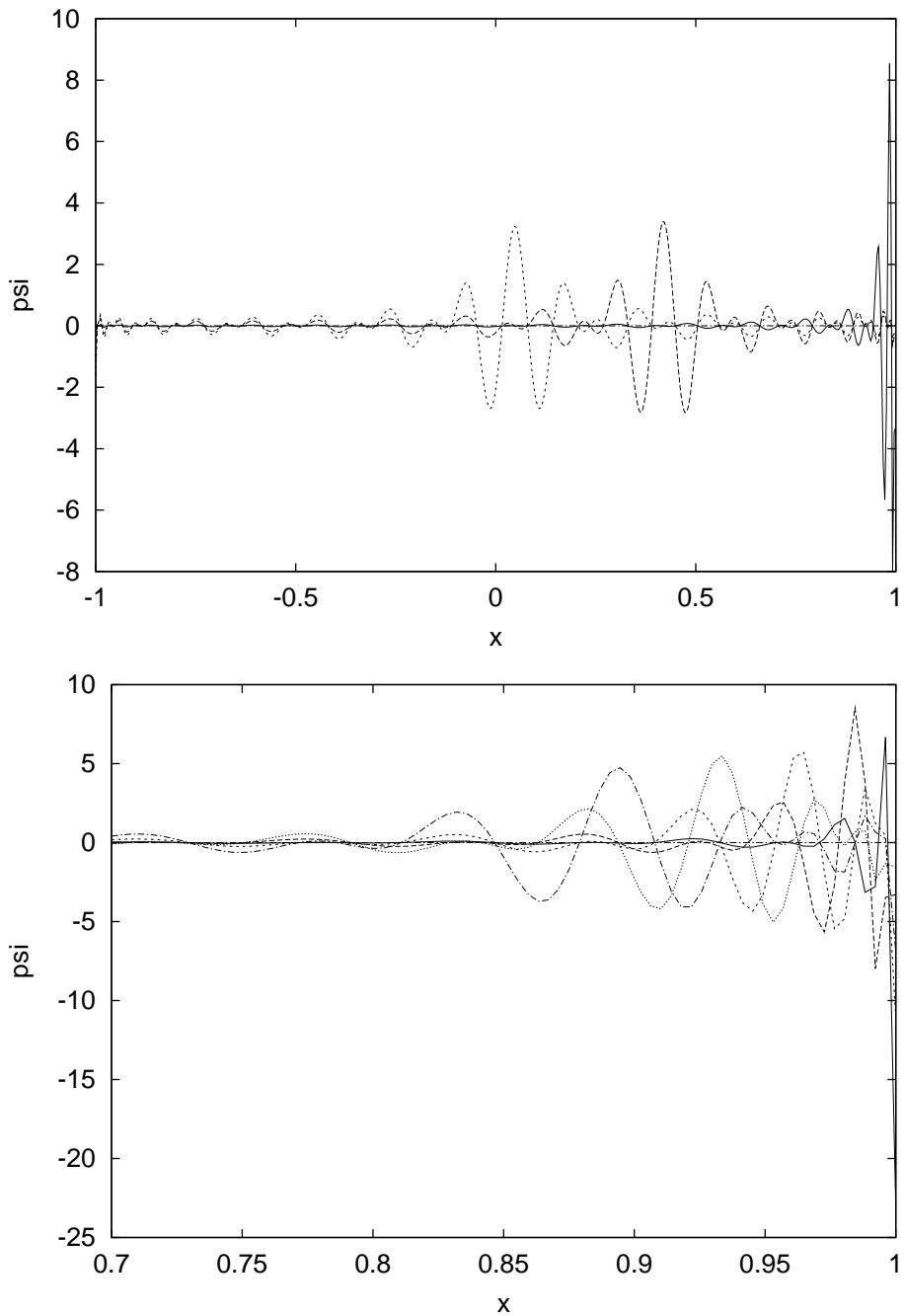


Figure 1: Wavelet functions of scale index $j = 5$ computed on a grid with $N = 512$ points. Position indices are $i = 16, 19, 29$ (top) and $i = 26, 27, 28, 29, 30$ (bottom). Observe that the abscissa of the lower plot is zoomed.

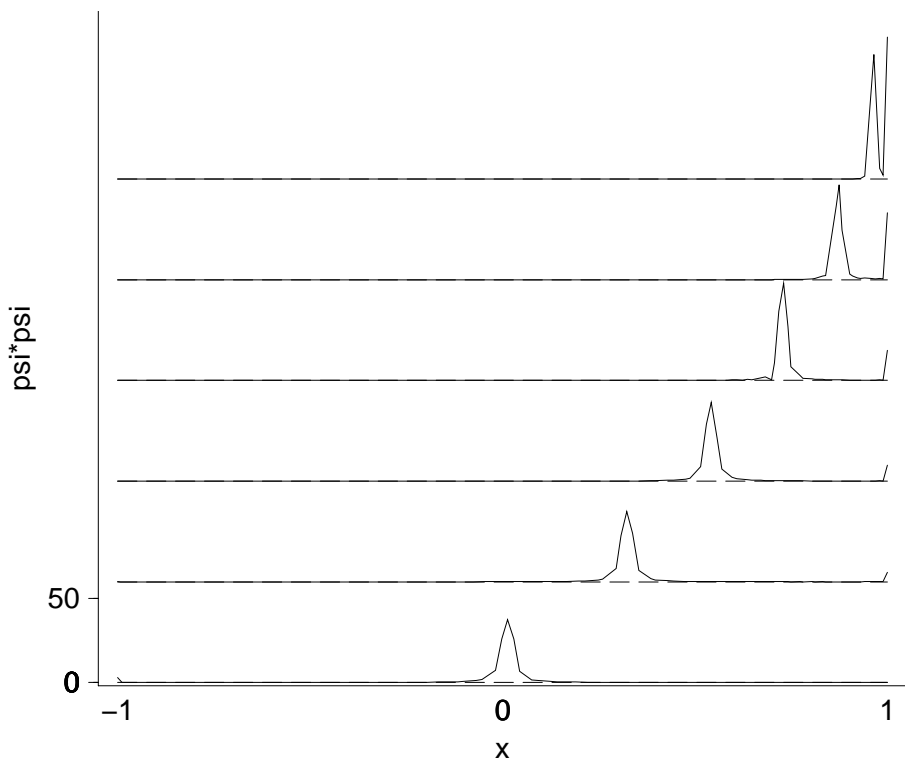
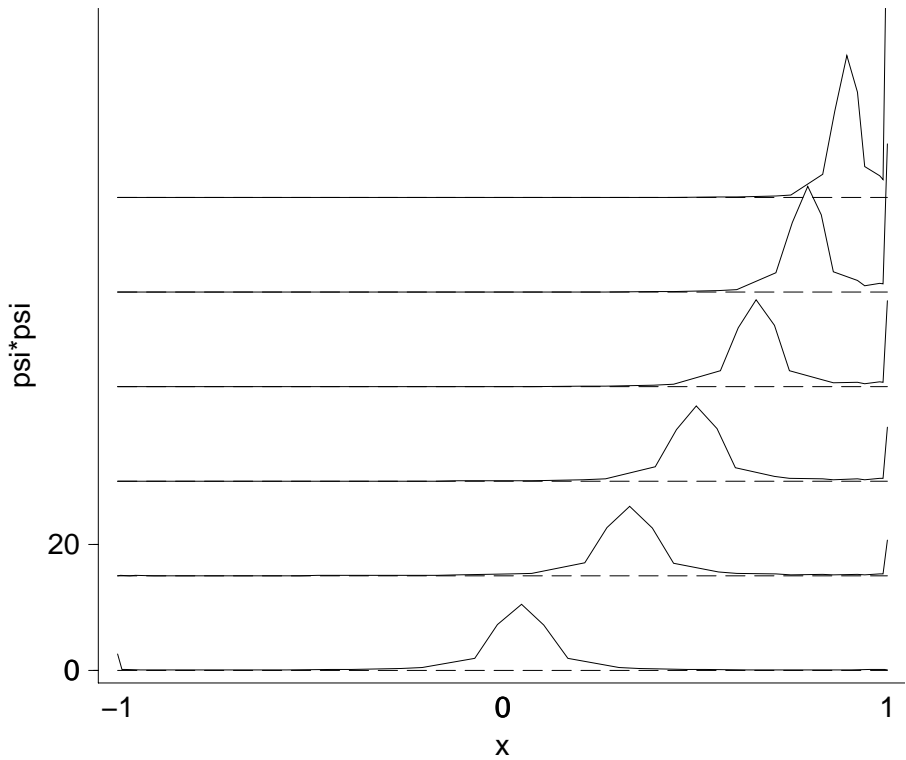


Figure 2: “Envelope” of the square of wavelet functions with scale index $j = 5$ (top) and $j = 7$ (bottom) for different center locations, i.e. $i = 16, 19, 21, 23, 25, 27$ (top) and $i = 64, 77, 87, 97, 107, 117$ (bottom) computed on a grid with $N = 512$ points.

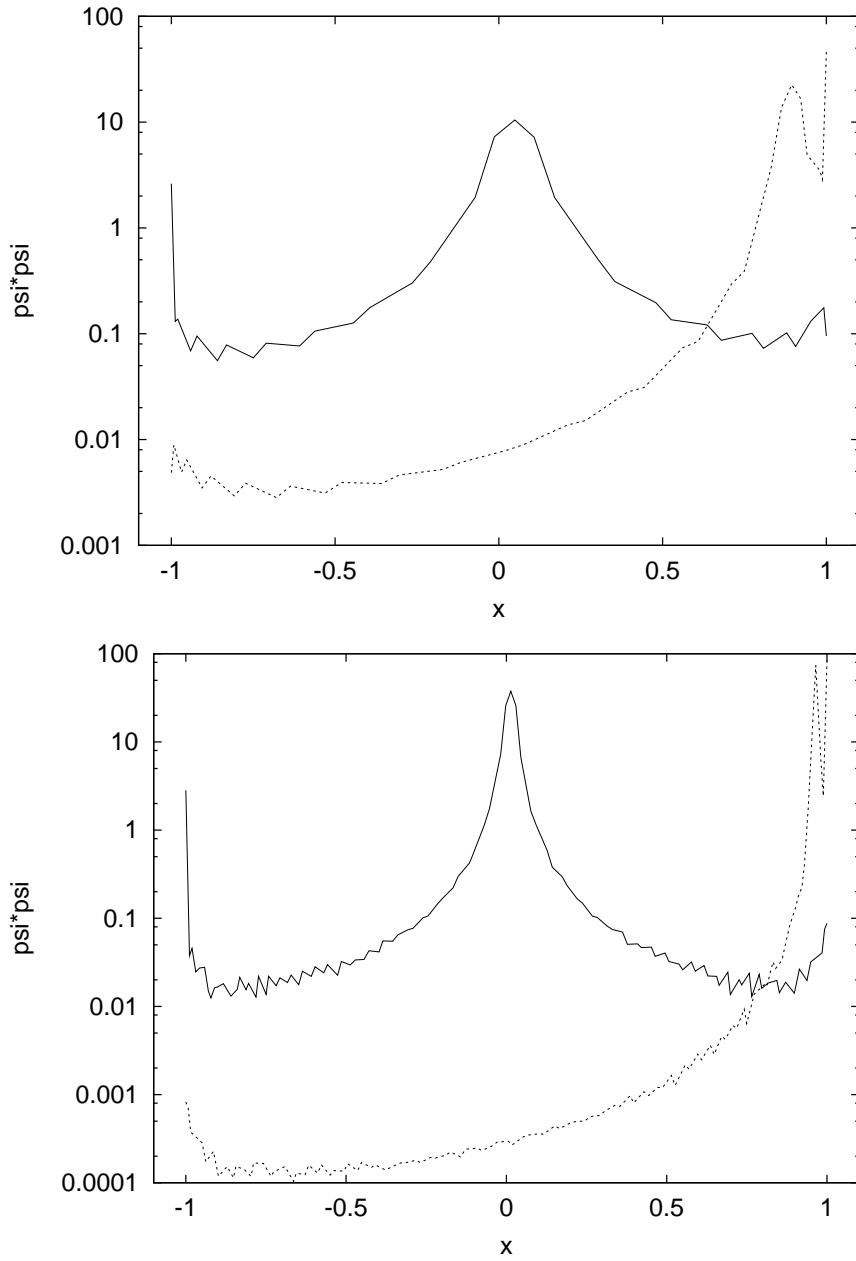


Figure 3: Log-lin plot of the “envelope” of the square of wavelet functions with scale index $j = 5$ (top) and $j = 7$ (bottom) in the center of the interval and close to the boundary i.e. $i = 15 = 6, 27$ (top) and $i = 64, 117$ (bottom) computed on a grid with $N = 512$ points.

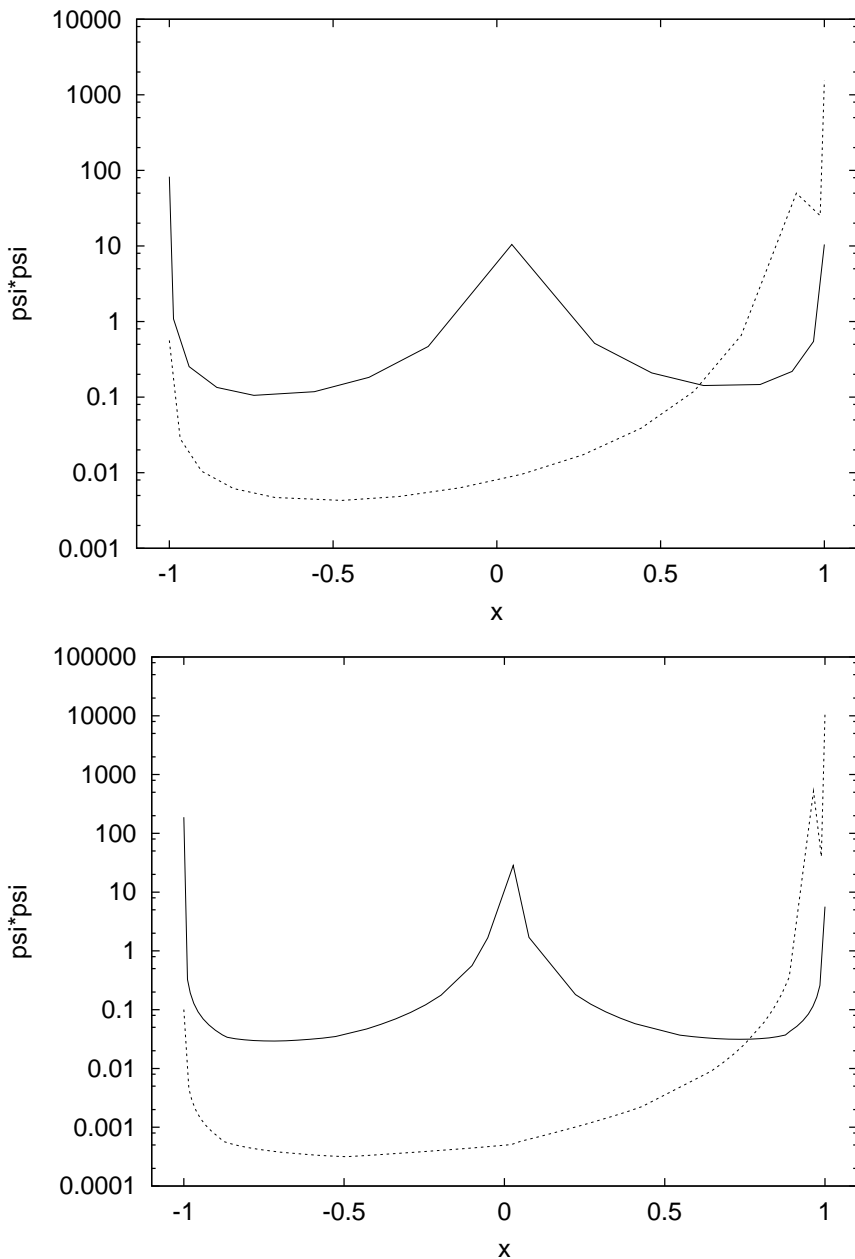


Figure 4: As Figure 3, but for the wavelet functions of [1], being based upon Chebyshev polynomials of the second kind instead of the present Legendre polynomials.

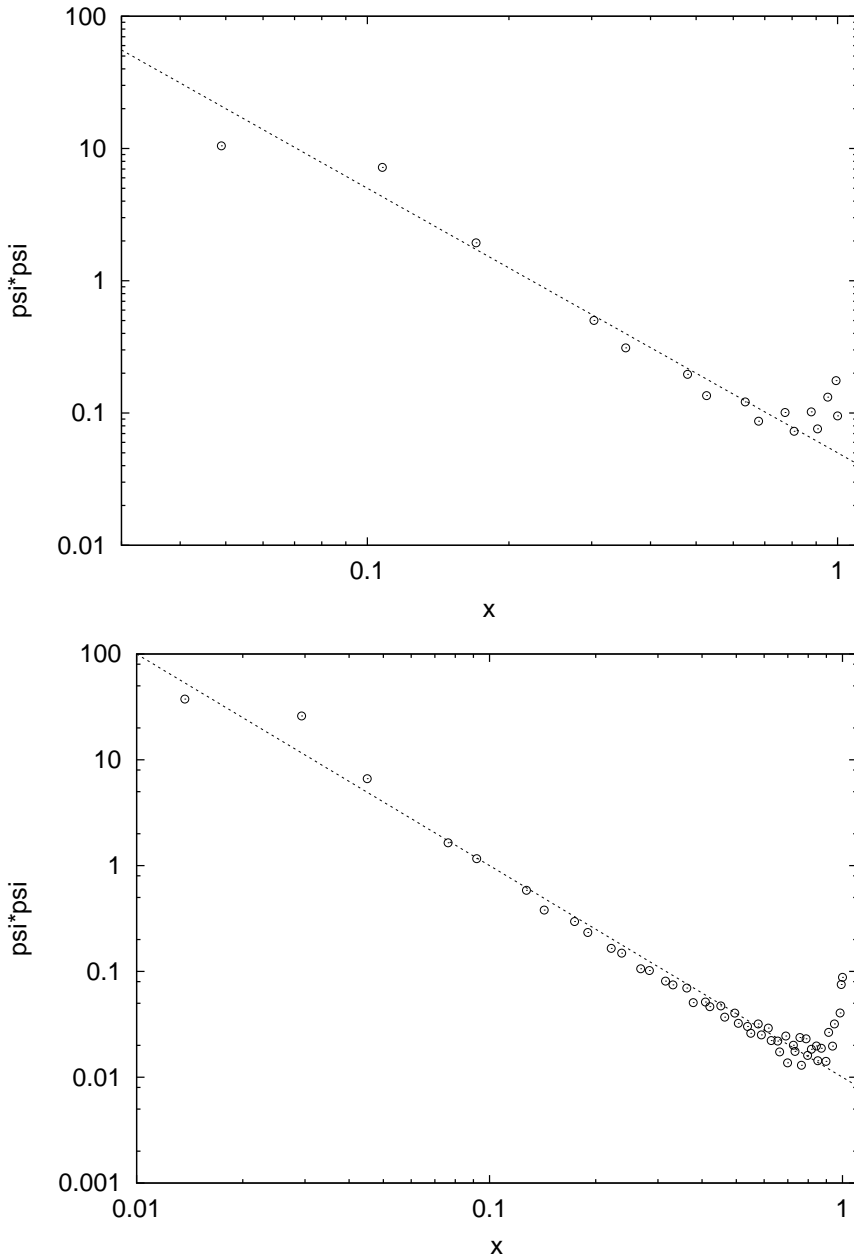


Figure 5: Log-log plot of the decay of the square of wavelet functions of degree $n = 32$ (top) and $n = 128$ (bottom) with center locations in the center of the interval. The straight line has a slope of -2 in both cases.

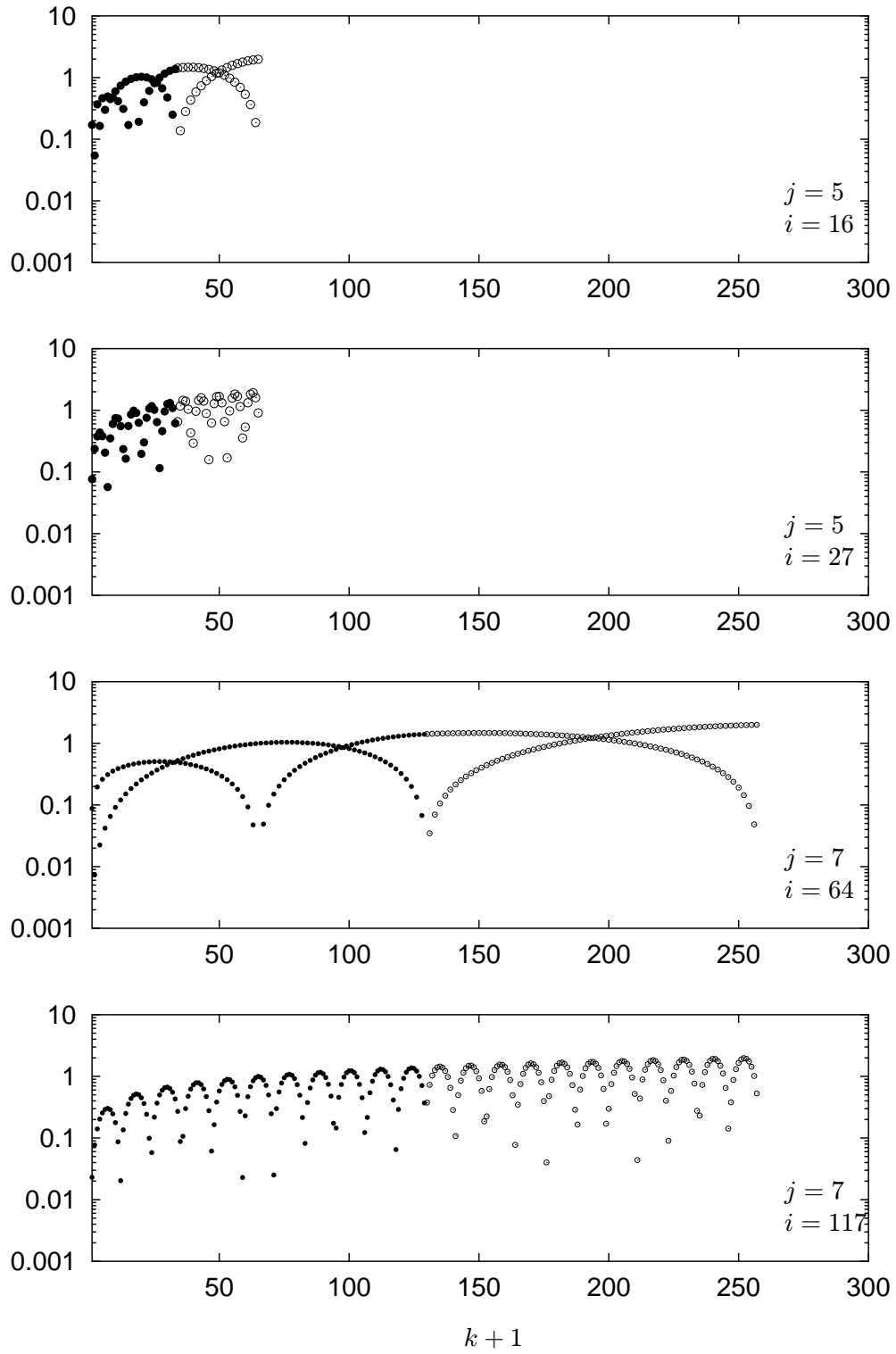


Figure 6: Lin-log plot of the absolute value of the Legendre spectral coefficients (as function of wavenumber k) of wavelet functions (open symbols) and scaling functions (filled symbols) of scale index $j = 5$ and $j = 7$ and $i = 16, 27$ (top) and $i = 64, 117$, respectively.

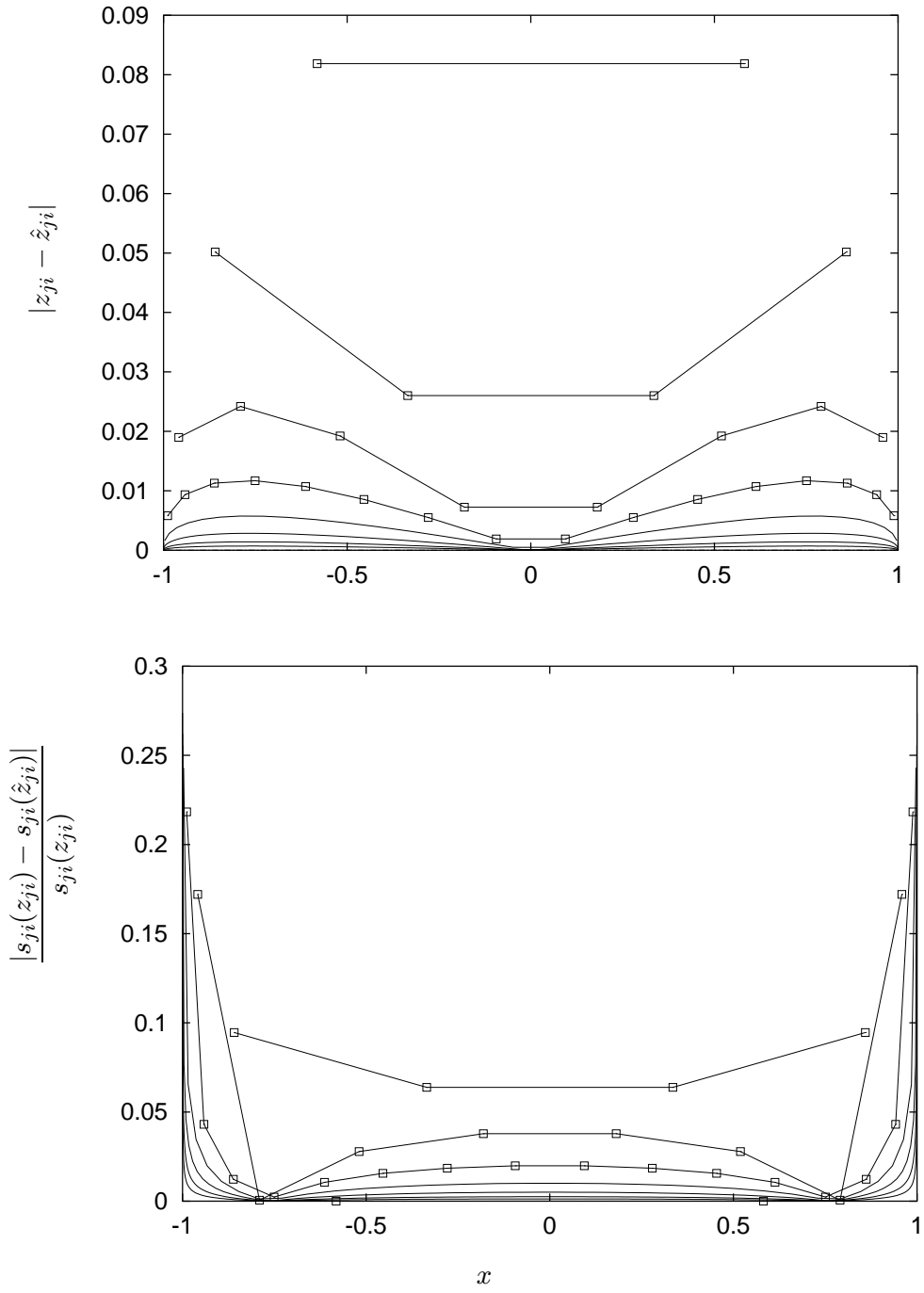


Figure 7: The difference in the definition of the center locations (top) and the physical scale parameter (bottom) corresponding to each wavelet ψ_{ji} of the present Legendre basis: $s_{ij}(\hat{z}_{ji})$ is the scale defined from the spatial variation of the Chebyshev roots \hat{z}_{ji} given in (14); $s_{ji}(z_{ji})$ is the value obtained by numerically computing the distance between neighboring centers z_{ji} of wavelets.

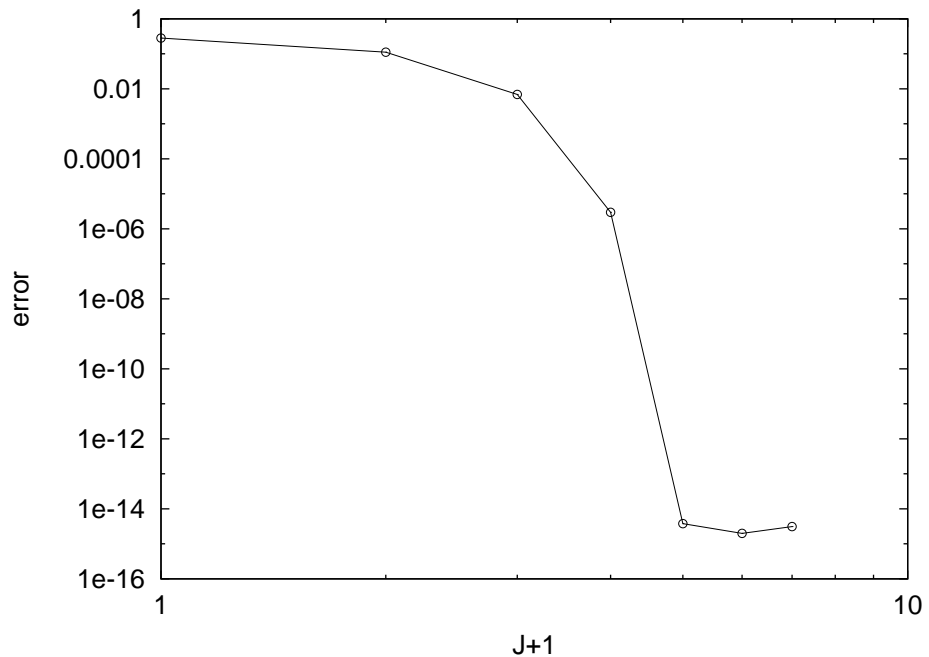


Figure 8: Convergence of the approximation when analysing the function $u(x) = \exp(-4x^2)$, the curve showing the maximum relative error as a function of the number of levels J used in the reconstruction. The r.m.s. error (not shown) has a similar behaviour.

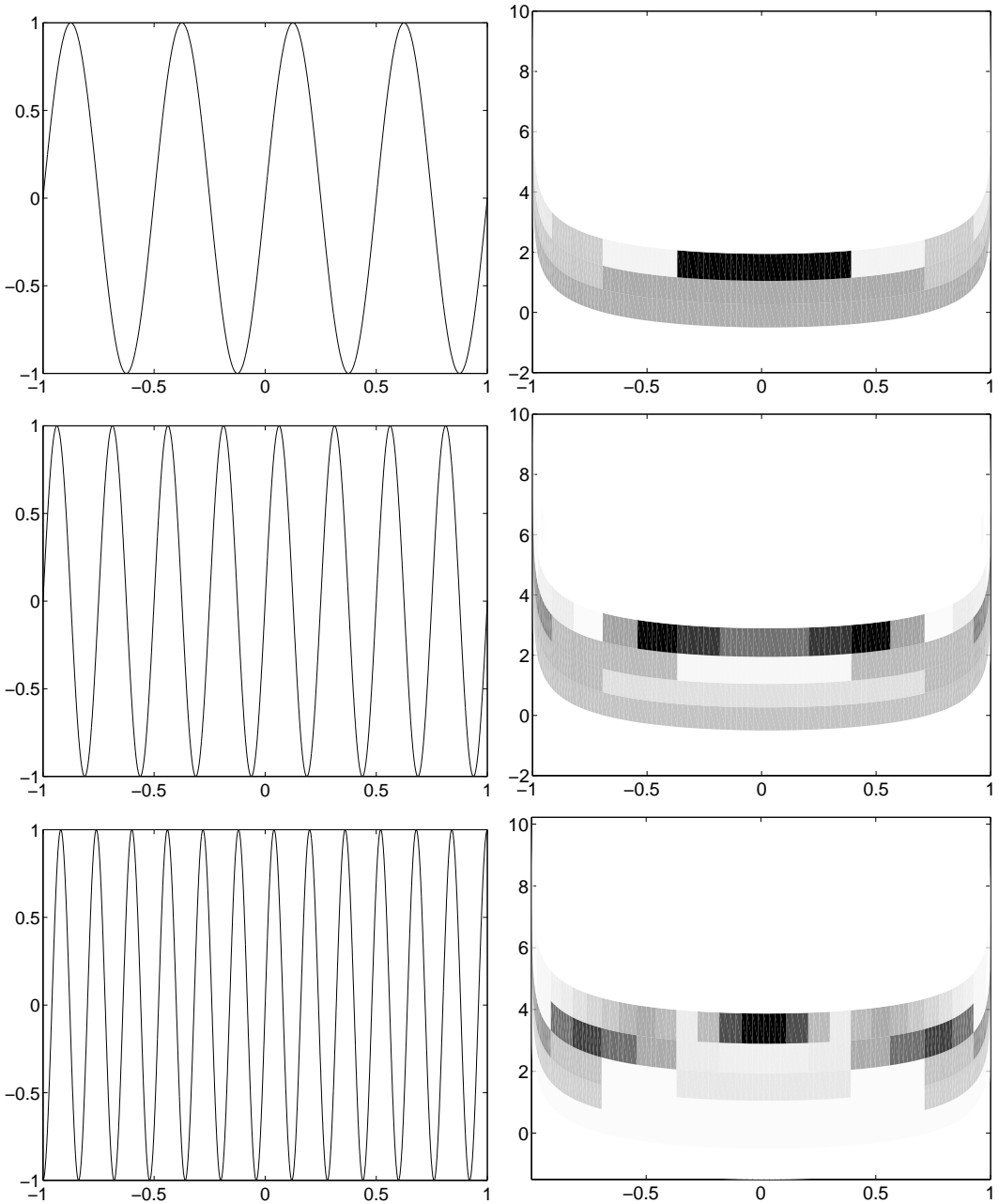


Figure 9: Wavelet transform of a periodic signal: $u(x) = \sin(2\pi x a)$ with $a = 2, 4, 6.25$ from top to bottom. The left column shows the signal; in the scalogram on the right the abscissa relates to the position in the domain $x \in [-1, 1]$ while the ordinate gives the inverse of the scale parameter in logarithmic scale, i.e. $-\log_2(s_{ji})$. Darker shading indicates higher (absolute) coefficient values on a linear scale. The total number of modes is $N + 1 = 257$.

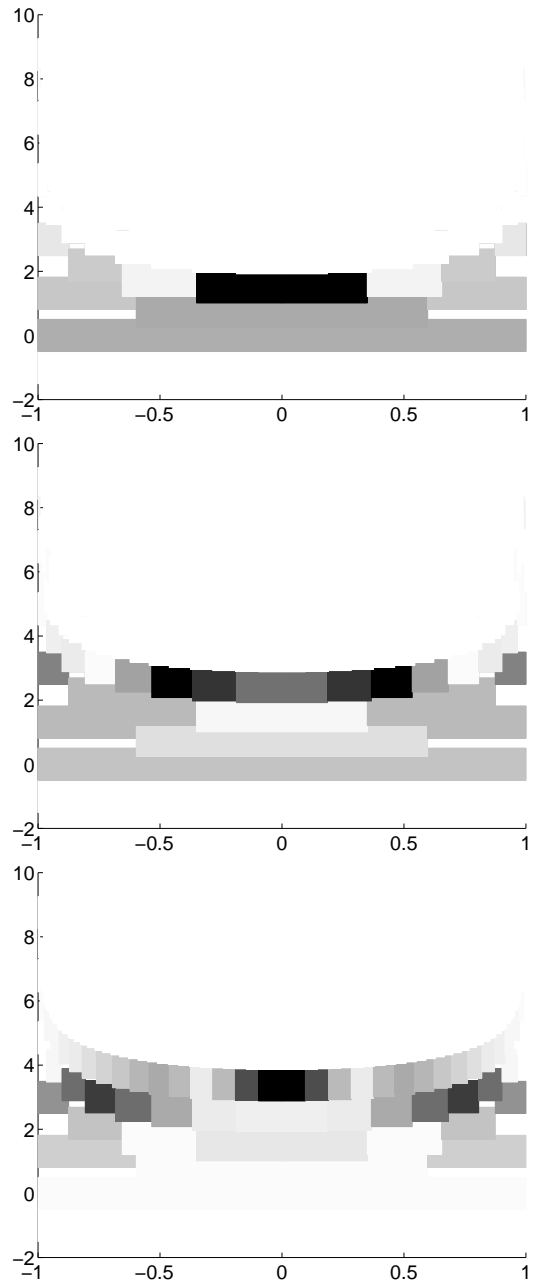


Figure 10: Coefficient scalograms as in Figure 9, but the scale is defined from the “exact”, numerically determined centers z_{ji}^ψ of the wavelets. Therefore, the visualization features “cells” which have a seemingly polygonal shape through overlapping and filled with the greyscale value according to the coefficients.

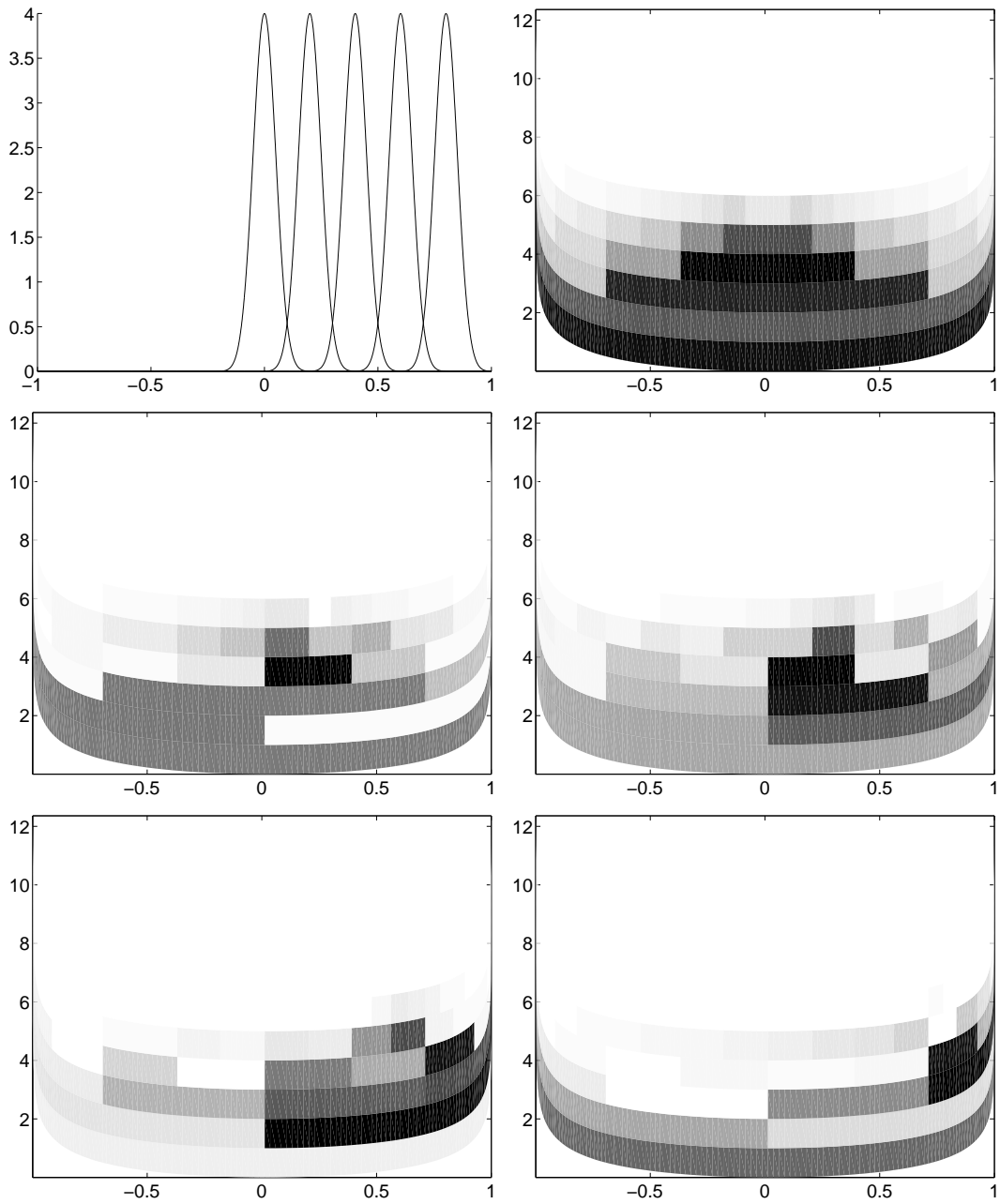


Figure 11: Wavelet transform of a single Gaussian bump: $u(x) = \exp(-((x - x_c)/(2\sigma))^2)$ with $\sigma = 0.05$ and the locations $x_c = 0.0, 0.2, 0.4, 0.6, 0.8$ from top to bottom and from left to right. Darker shading indicates higher (absolute) coefficient values on a linear scale. The abscissa relates to the position in the domain $x \in [-1, 1]$ while the ordinate gives the inverse of the scale parameter in logarithmic scale, i.e. $-\log_2(s_{ji})$. The total number of modes is $N + 1 = 257$.

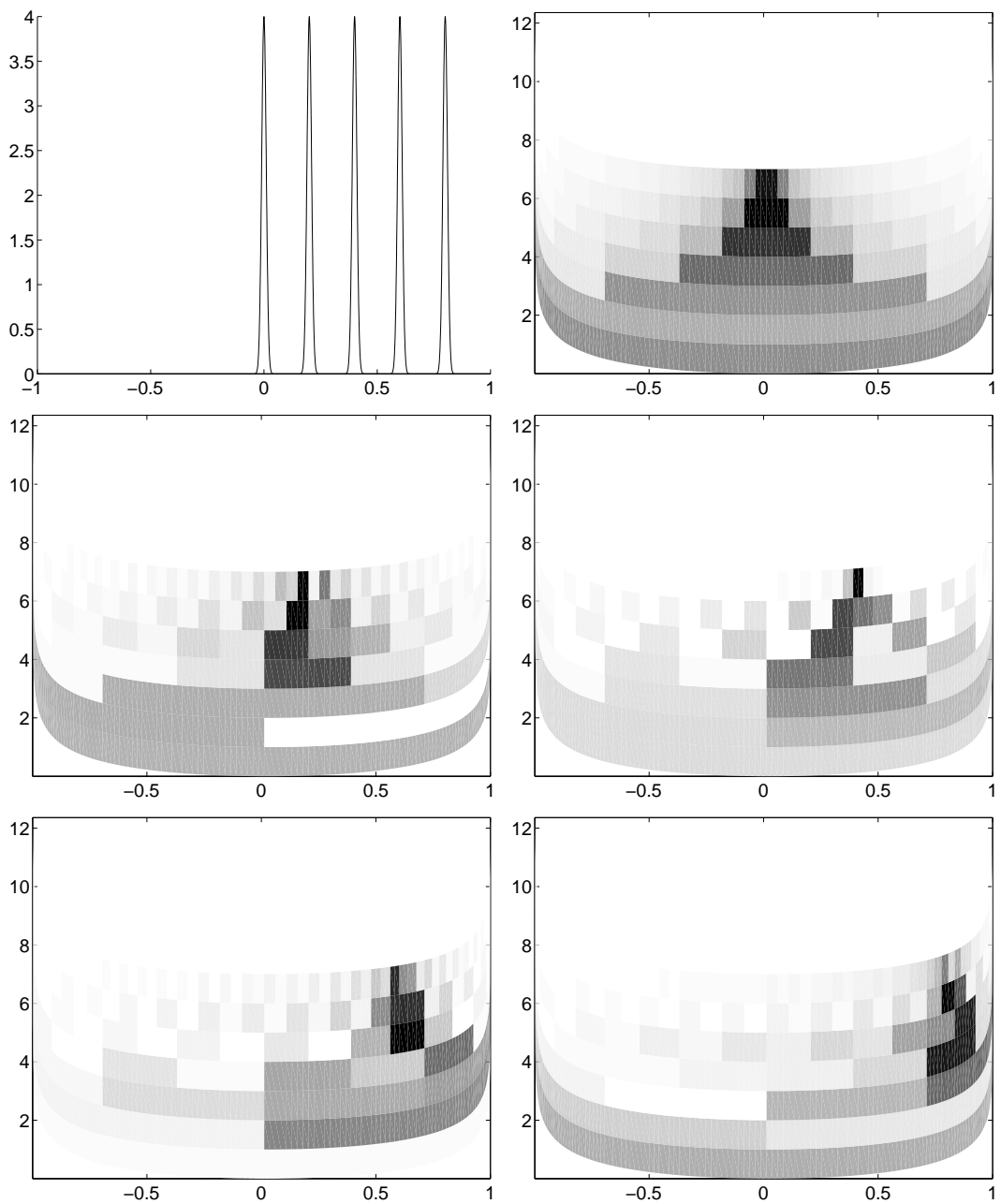


Figure 12: As Figure 11, but the signal being a narrower bump with $\sigma = 0.01$.

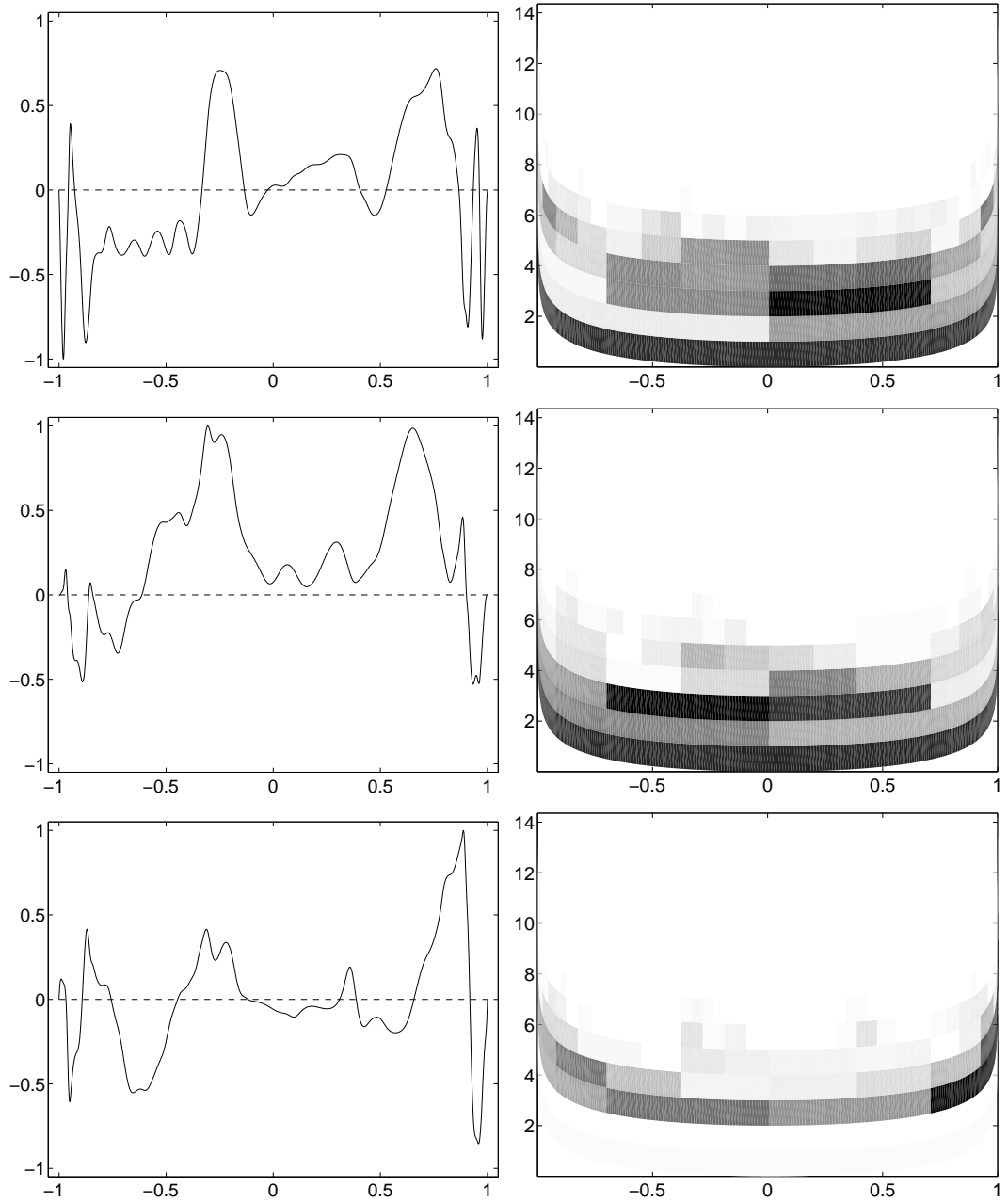


Figure 13: Wavelet coefficient diagram of the transformation of a fluctuation velocity signal from a turbulent channel flow at friction velocity Reynolds number $Re_\tau = 590$. The profiles on the left are taken across the channel, extending from wall to wall. Streamwise (top), wall-normal (middle) and the spanwise (bottom) instantaneous fluctuations, respectively. Each signal has been normalized such that its maximum absolute value is unity.

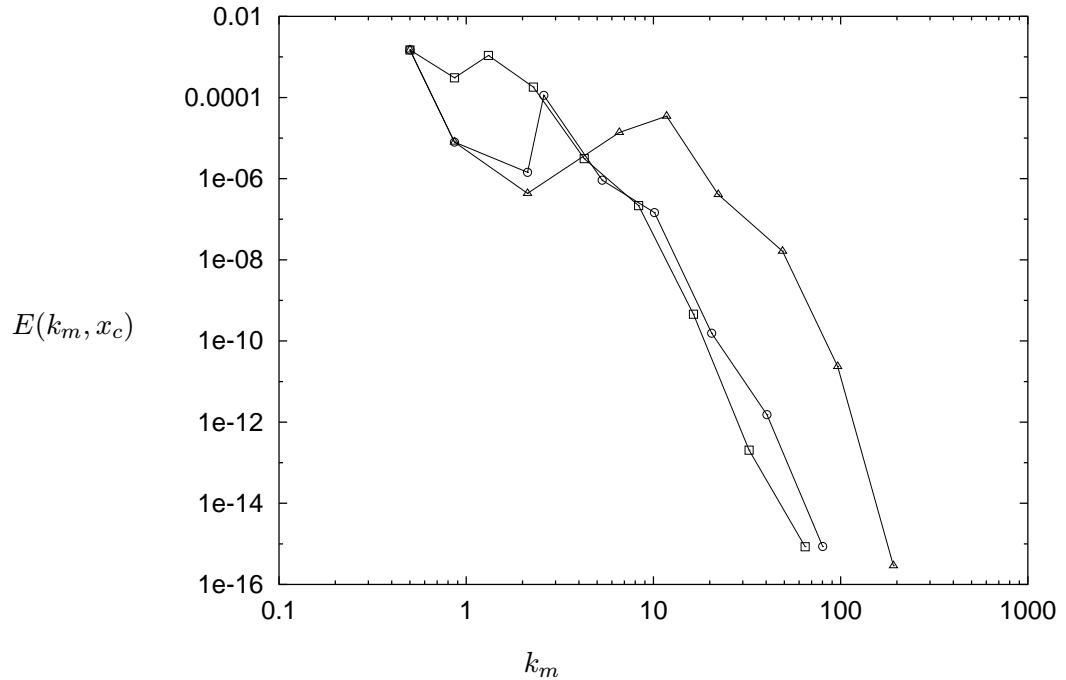


Figure 14: Local wavelet spectra $E(k_m, x_c)$ as a function of the inverse of the physical scale parameter $k_m = 1/s_{ij}$ corresponding to the streamwise velocity data of Figure 13 and taken at the following positions within the interval $x \in [-1, 1]$: \square , $x_c = 0.1$; \circ , $x_c = -0.6$; \triangle , $x_c = -0.94$.

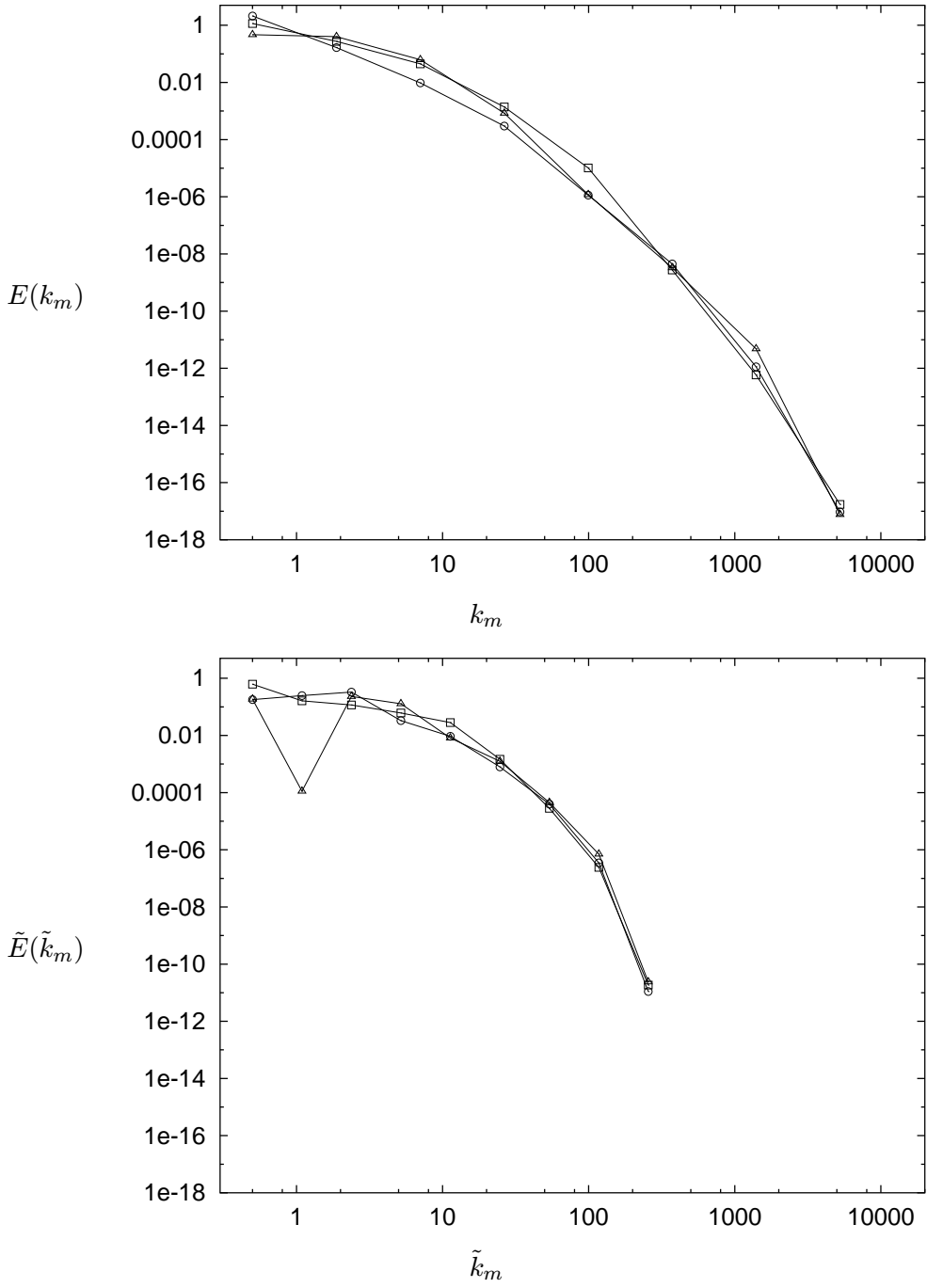


Figure 15: The global wavelet spectrum $E(k_m)$ (top) as a function of the inverse of the physical scale parameter $k_m = 1/s_{ij}$ corresponding to the transform of the data from turbulent channel flow. The bottom figure shows the Legendre coefficient spectrum $\tilde{E}(\tilde{k}_m)$. In both cases, the values of the spectrum are accumulated over logarithmically-spaced bins and normalized such that their integral amounts to unity. \square , streamwise fluctuations; \circ , wall-normal; \triangle , spanwise.

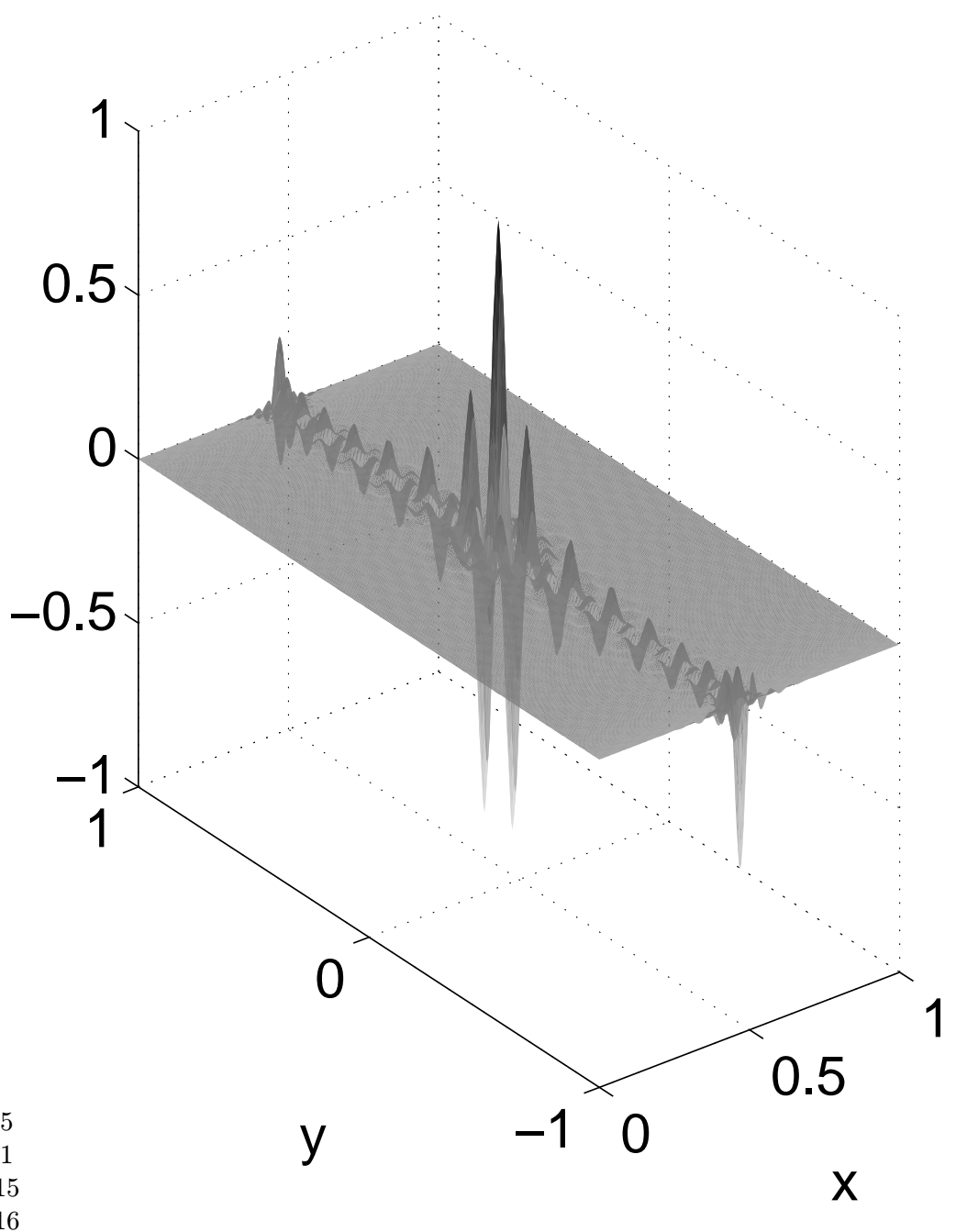


Figure 16: Illustration of the basis functions of the two-dimensional MRA, sampled on a grid with 256^2 points.

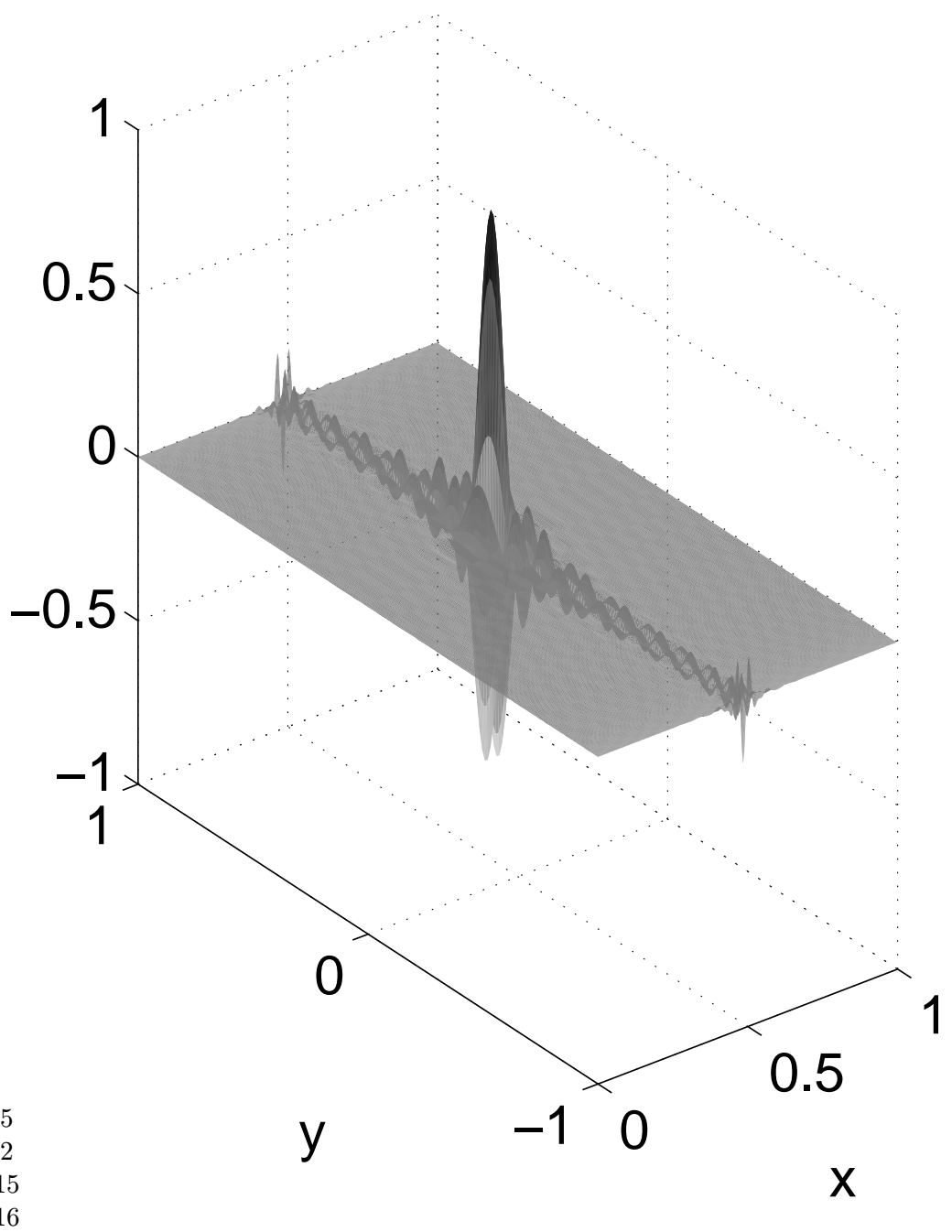


Figure 16: (continued)

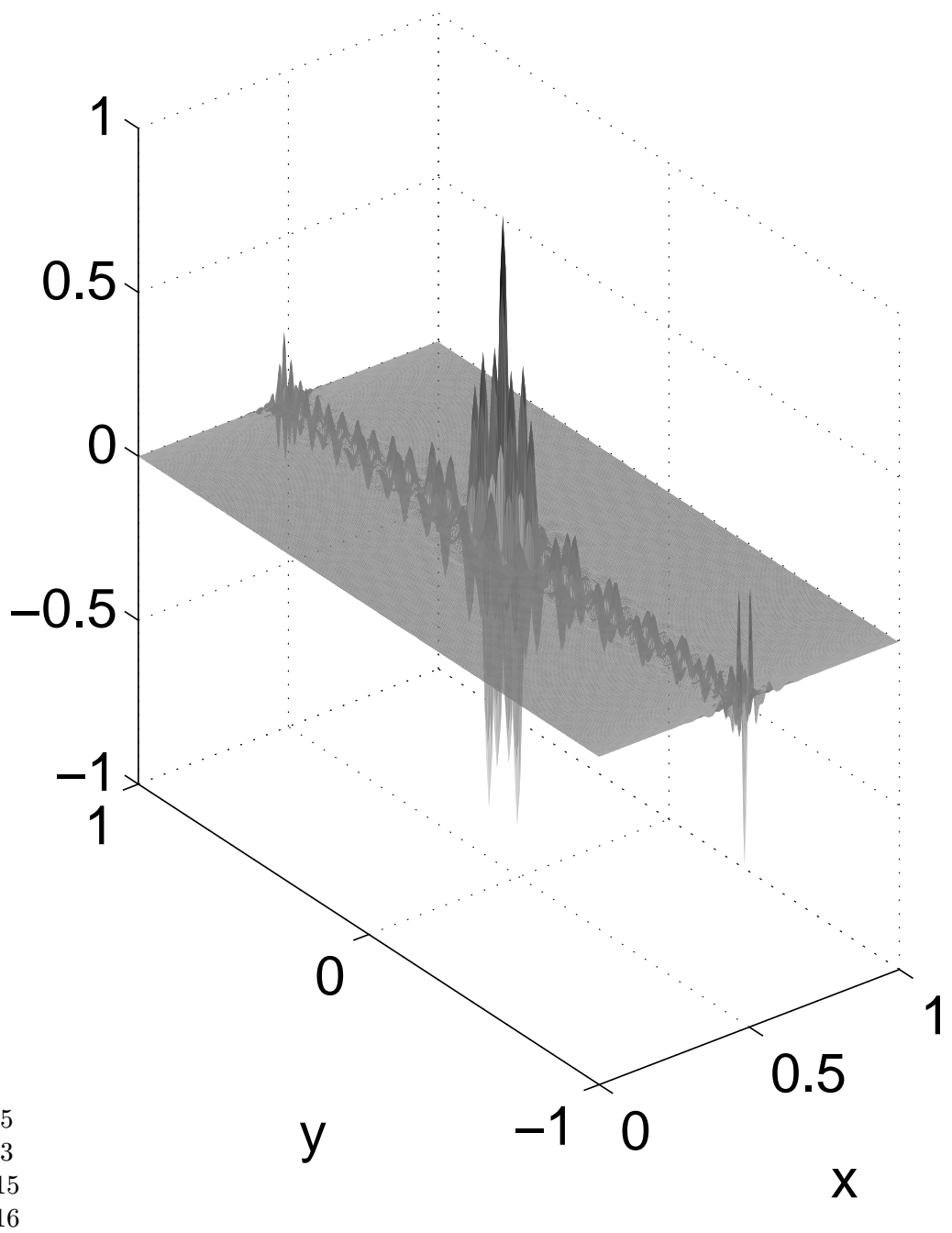


Figure 16: (continued)

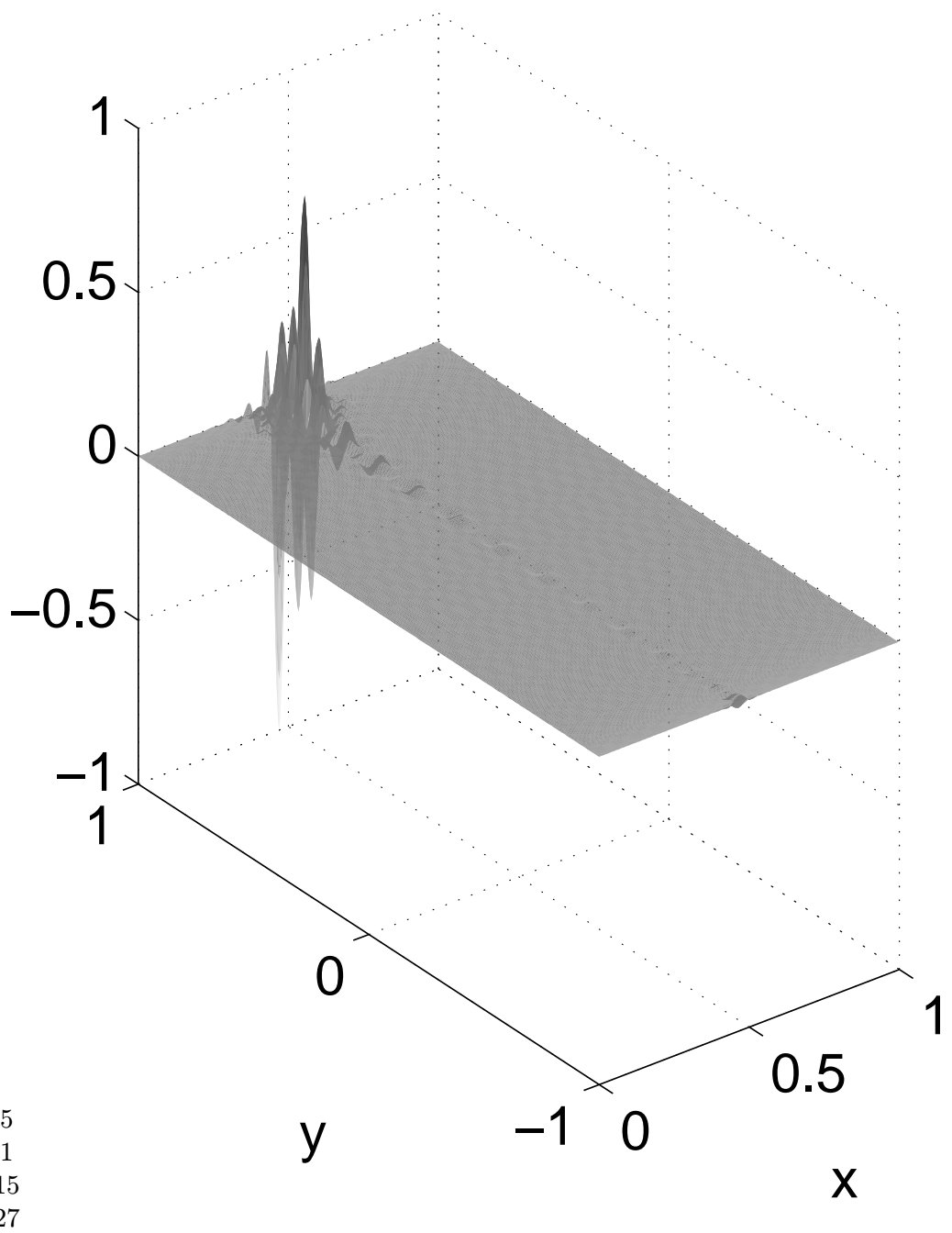


Figure 16: (continued)

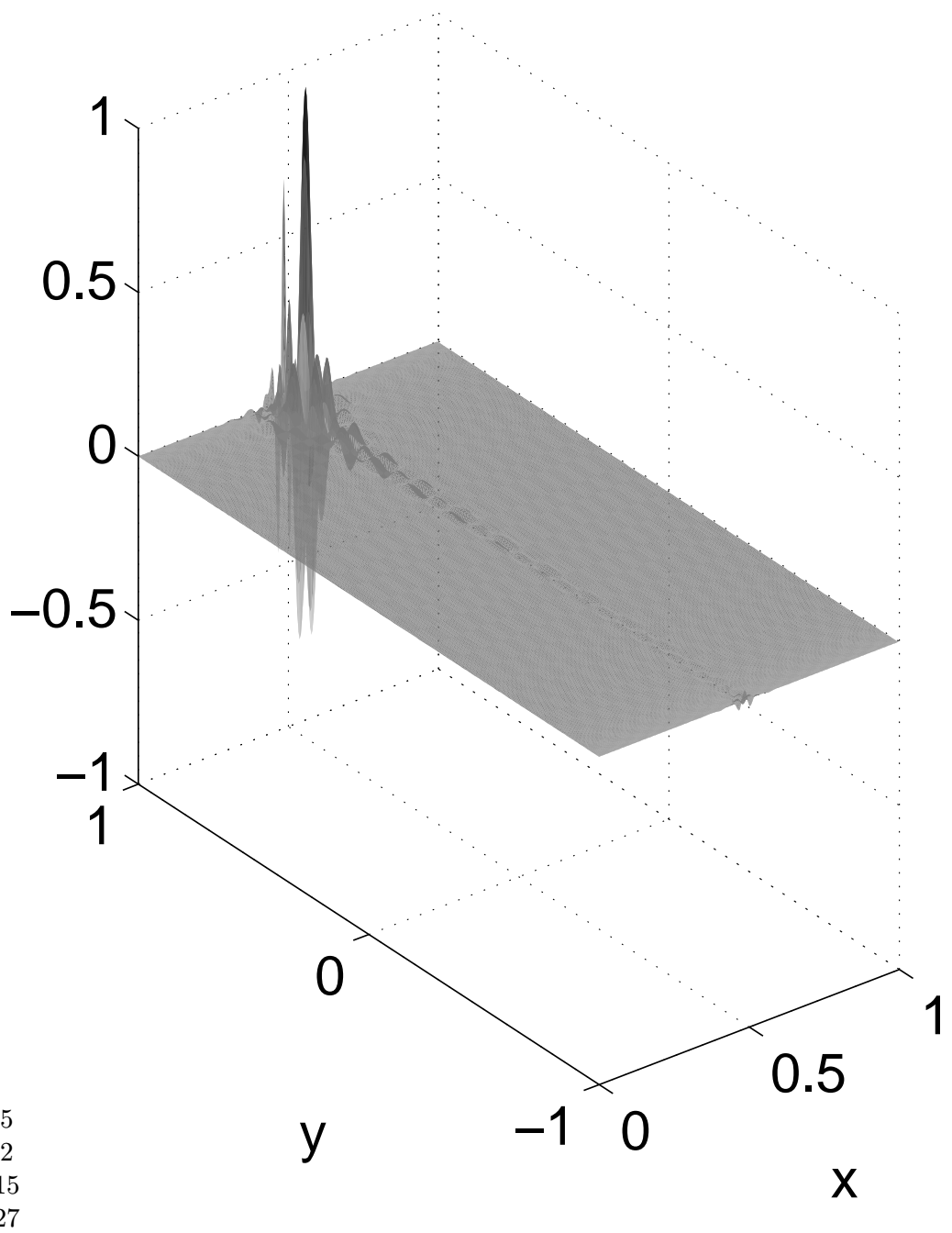


Figure 16: (continued)

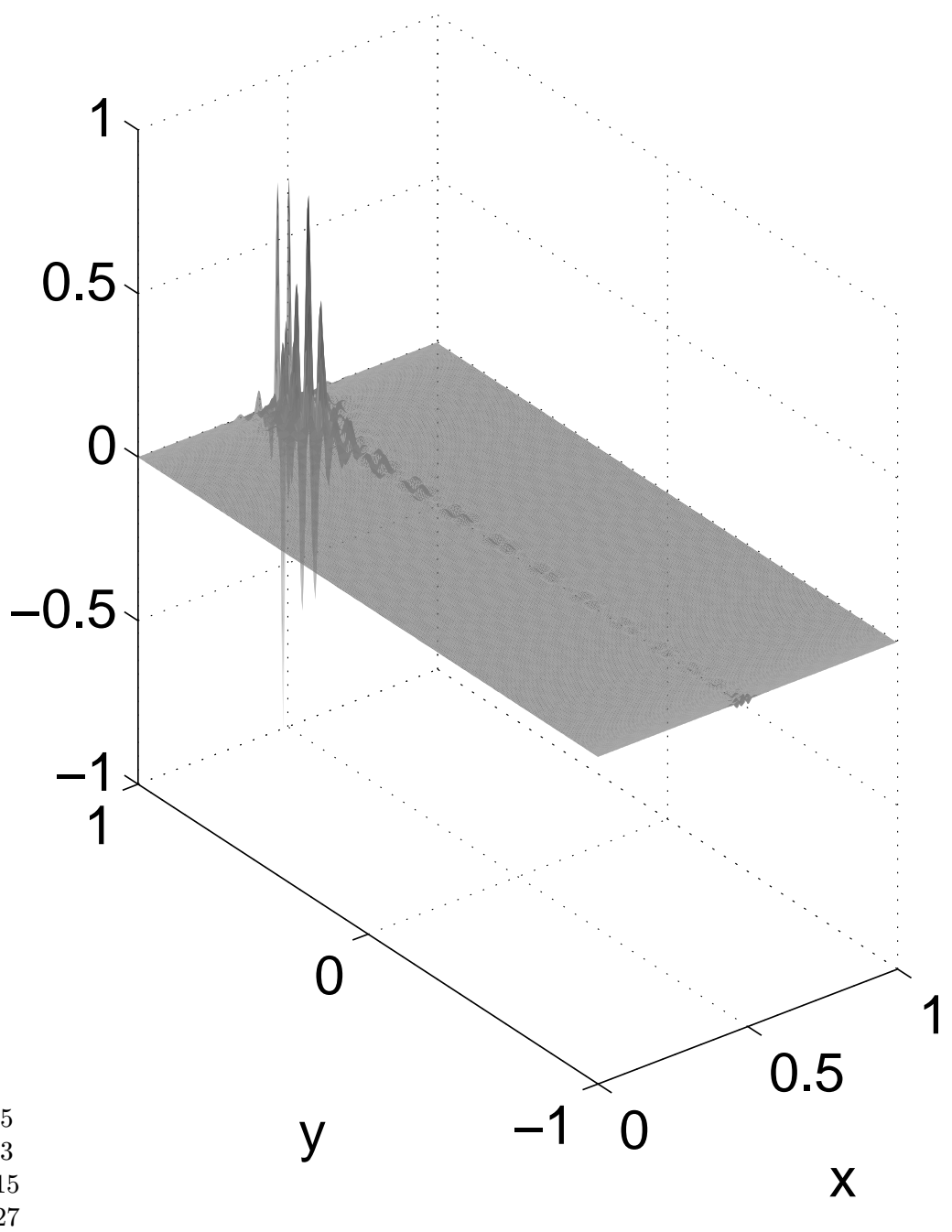


Figure 16: (continued)

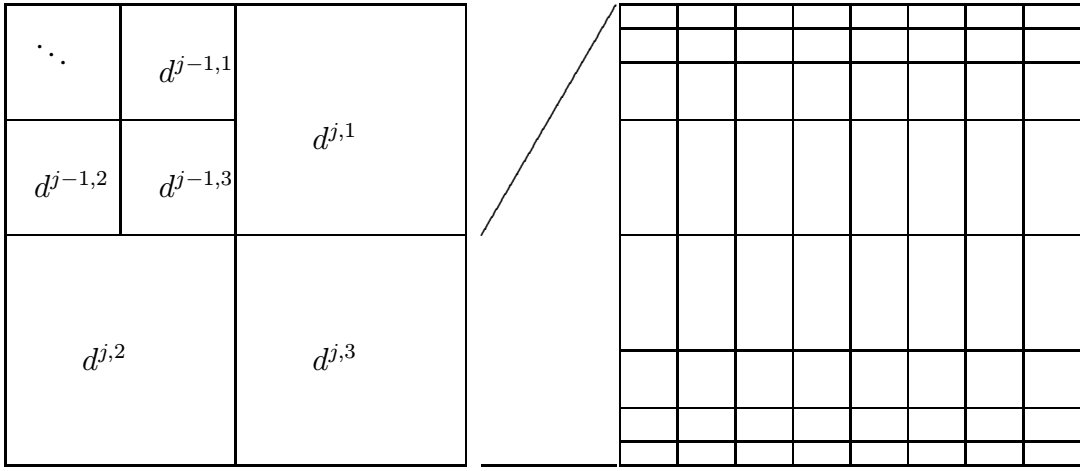


Figure 17: The graphical representation of the wavelet coefficients of the two-dimensional MRA. The enlargement on the right shows that the individual colored cells of each block of data (coefficients which have common j and q indices) are uniformly spaced in the horizontal direction and spaced according to the approximate definition of the Legendre wavelet centers in (15) in the vertical direction. Note that the position of $d^{j,2}$ and $d^{j,1}$ is as proposed in [8] and therefore interchanged with respect to [5, p.315].

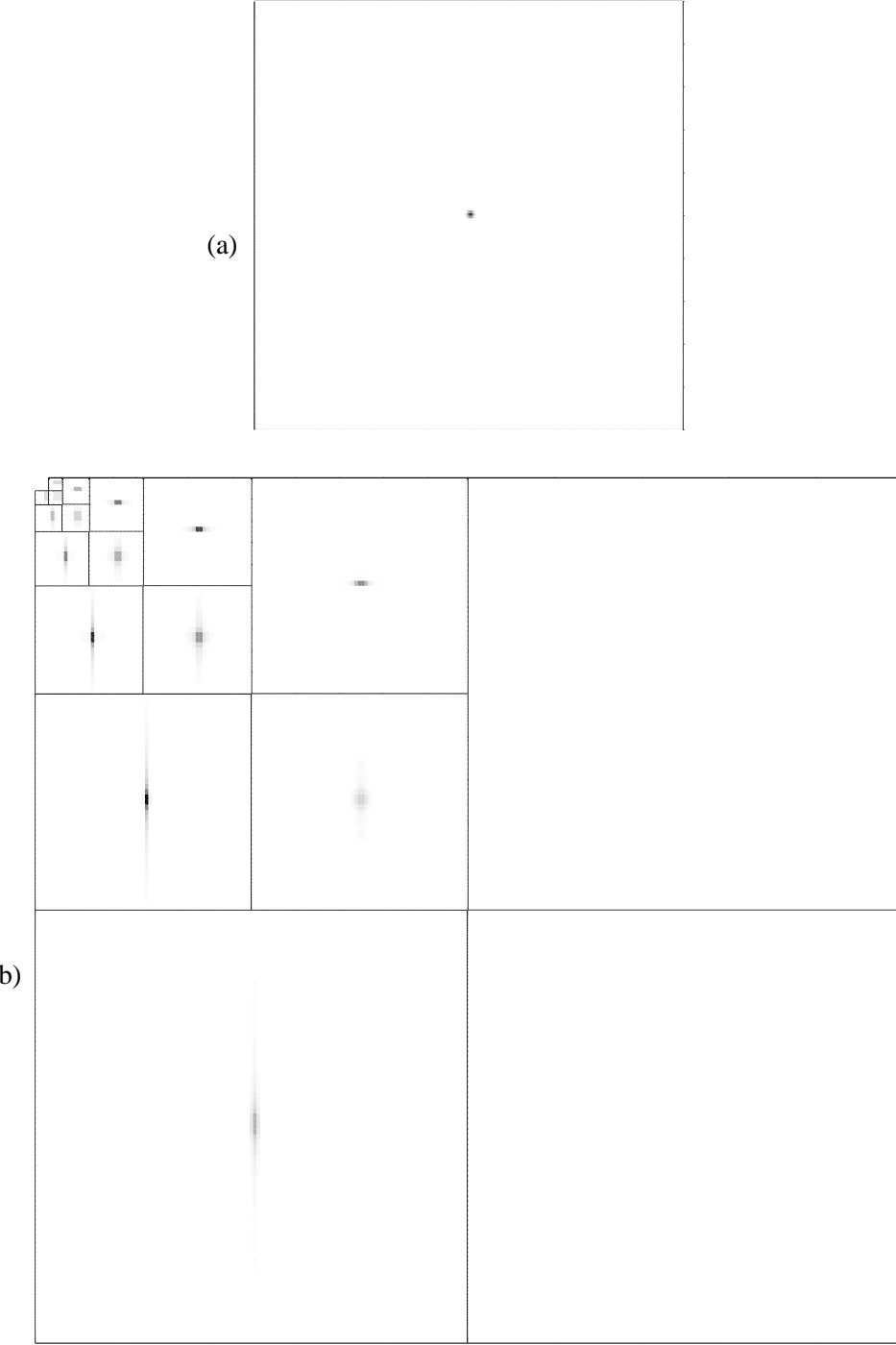
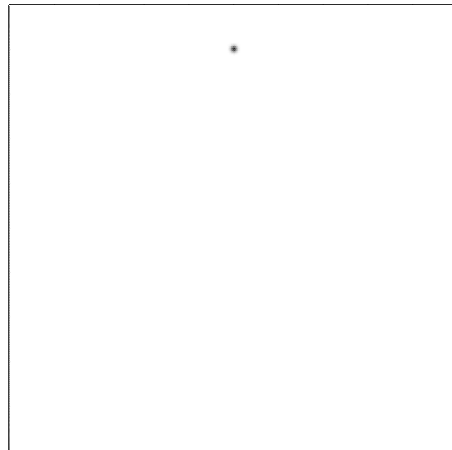


Figure 18: The wavelet transform of a two-dimensional single gaussian bump, $u(x, y) = \exp(-((x - x_c)^2 + (y - y_c)^2)/(2\sigma)^2)$ with $\sigma = 0.01$ and the locations $y_c = 0.5$, $x_c = 0.0, 0.8, 0.95$. The top graph (a) shows the signal, the bottom graph (b) shows the absolute value of the wavelet coefficients at scale indices $2 \leq j \leq 6$; the numerical grid has a dimension of $N = 2^8$. The greyscale is linear from zero (white) to the maximum absolute coefficient value over all j , q , i_x and i_y (black).

(a)



(b)

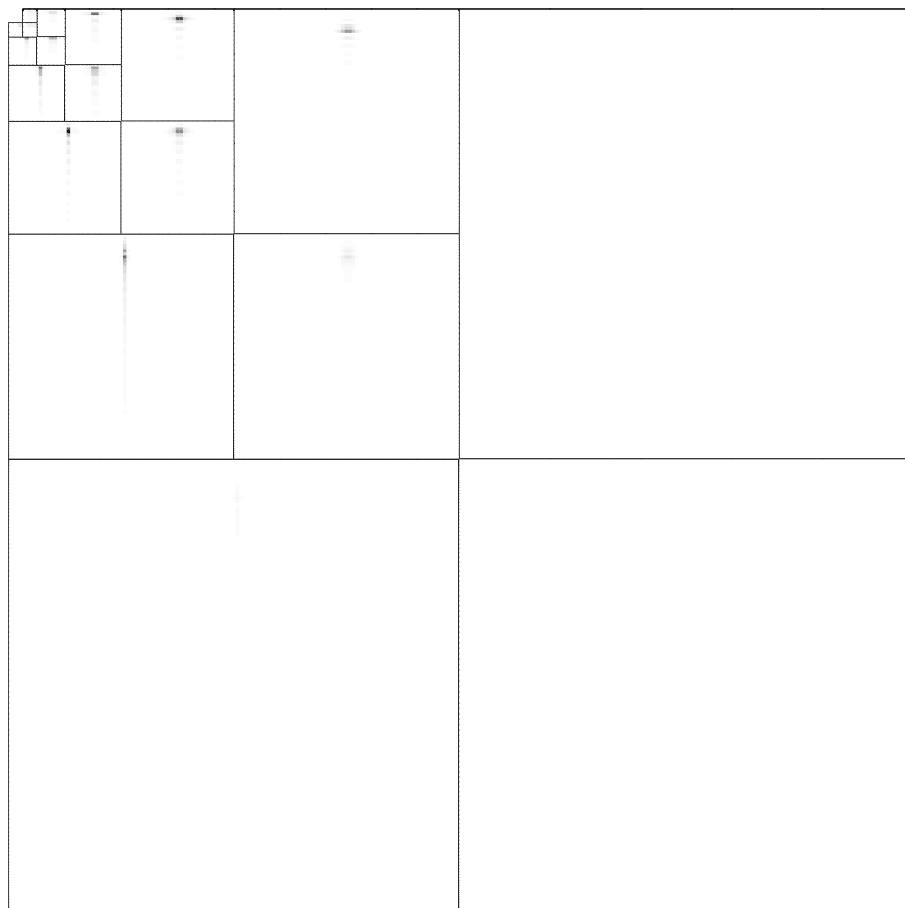
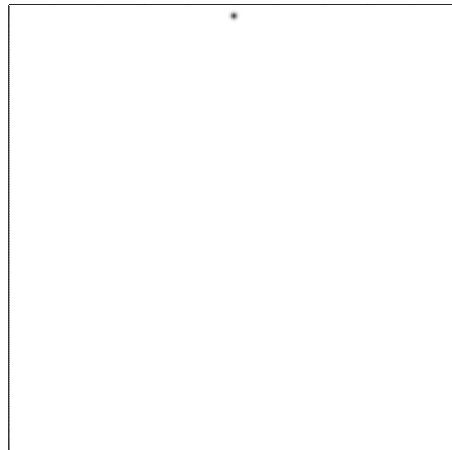


Figure 18: (continued)

(a)



(b)

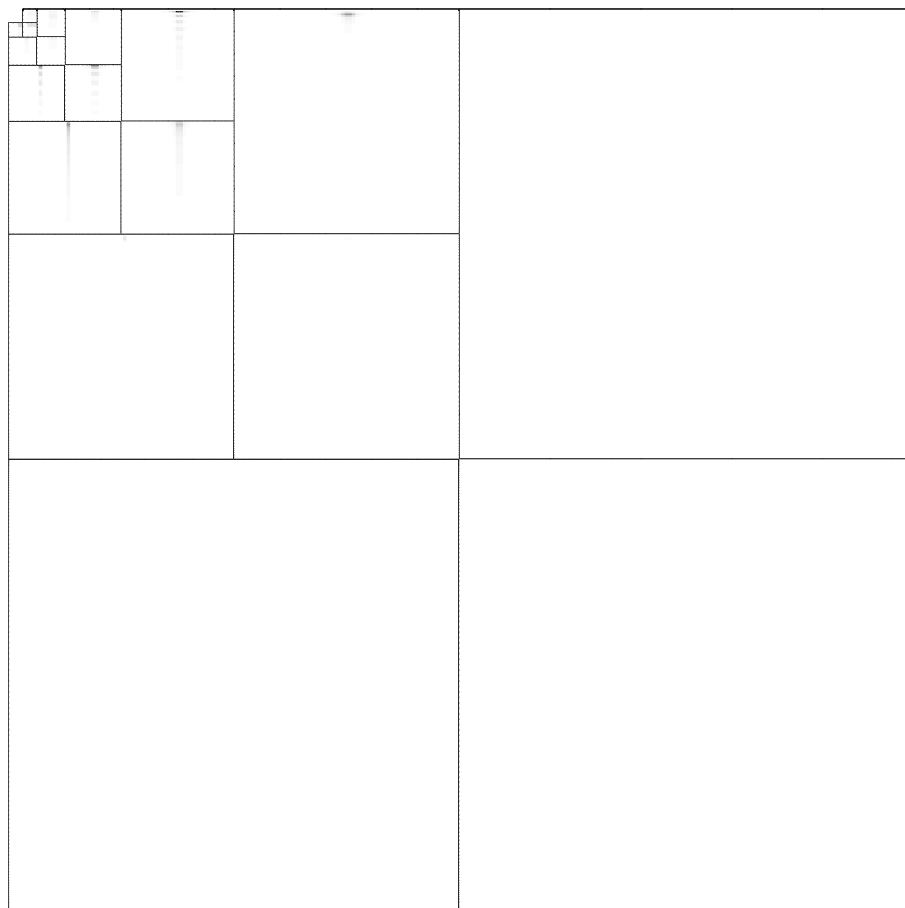


Figure 18: (continued)

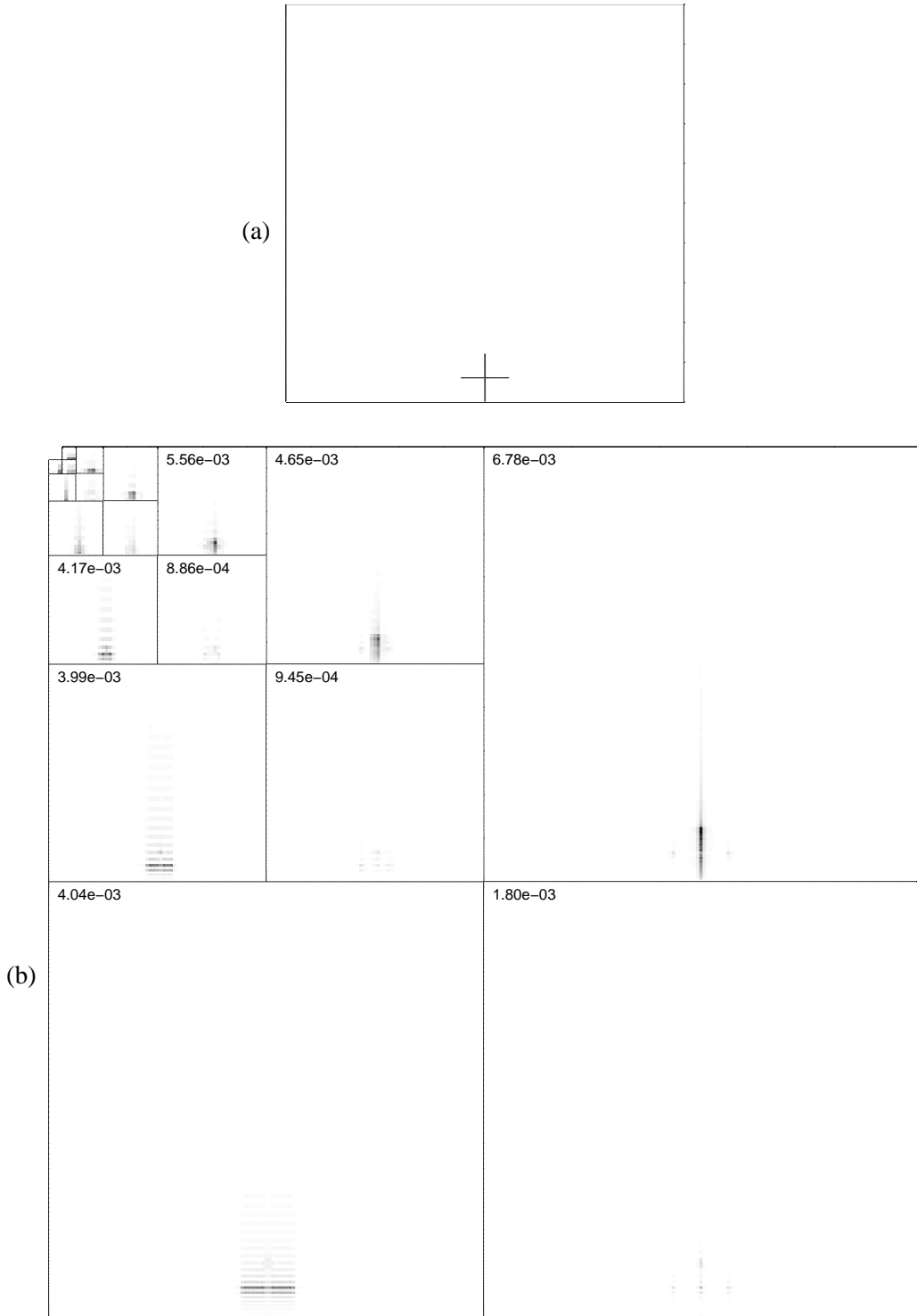


Figure 19: The transform of a cross-shaped binary signal close to the lower boundary of the domain. The top graph (a) shows the signal, the bottom graph (b) shows the absolute value of the wavelet coefficients at scale indices $2 \leq j \leq 7$. The numerical grid has a dimension of $N = 2^8$. The greyscale is linear from zero (white) to the maximum absolute coefficient value over all j, q, i_x and i_y (black). The numerical values indicate the maximum value occurring in each data block with given values of j and q .

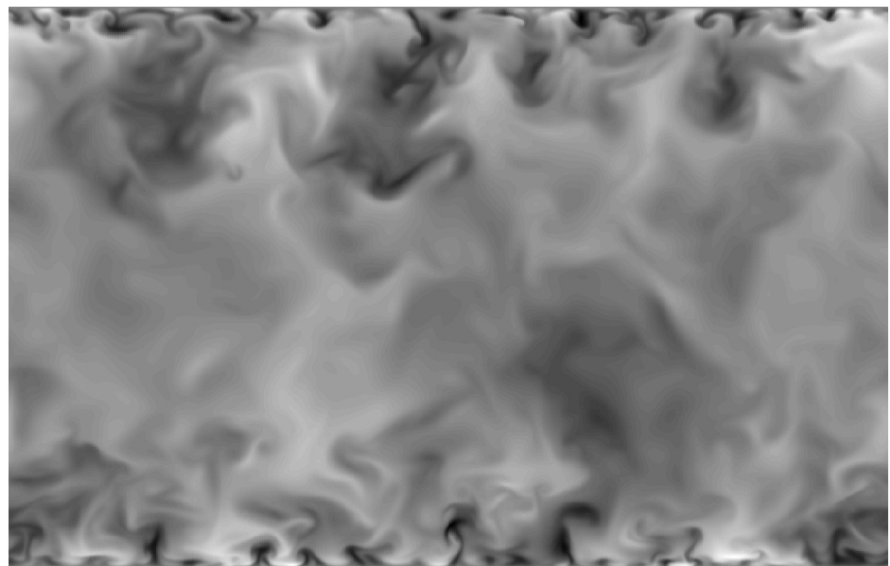


Figure 20: Streamwise velocity fluctuations of a snapshot from a turbulent channel flow at friction velocity Reynolds number $Re_\tau = 590$. The plane is spanwise/wall-normal, i.e. the mean flow is perpendicular to the plane. The aspect ratio reflects the physical size of the domain.

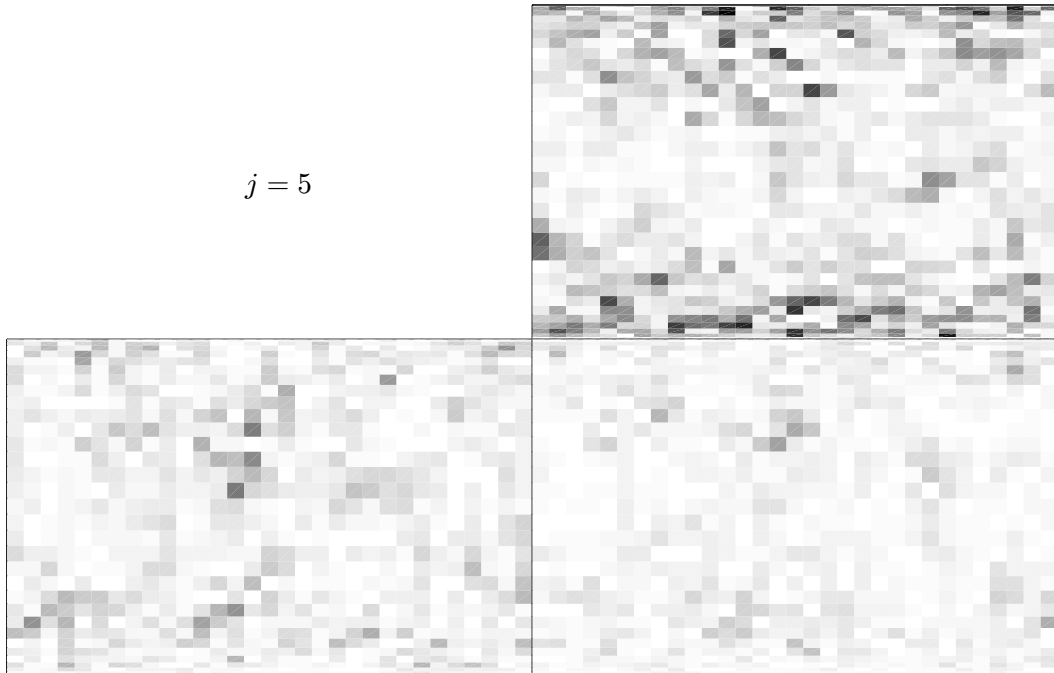


Figure 21: The absolute value of the wavelet coefficients of the transform of streamwise velocity fluctuations in a turbulent channel flow at friction velocity Reynolds number $Re_\tau = 590$. The plane is spanwise/wall-normal. The graphs show the scale indices $5 \leq j \leq 7$; the numerical grid has a dimension of $N = 2^9$. The greyscale coloring is chosen such that white corresponds to zero intensity and black to maximum intensity. This scale is adjusted independently for each level j .

$j = 6$

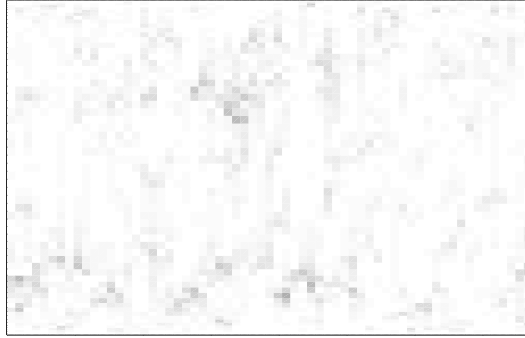
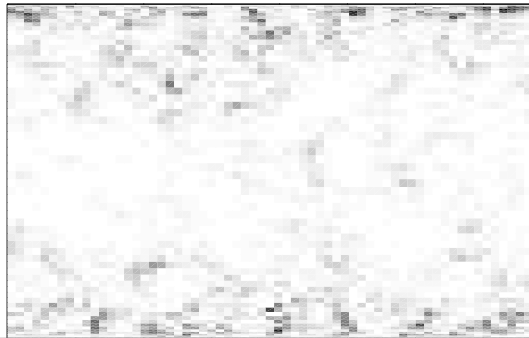


Figure 21: (continued)

$j = 7$



Figure 21: (continued)

$j = 8$



Figure 21: (continued)

PIK Report-Reference:

- No. 1 3. Deutsche Klimatagung, Potsdam 11.-14. April 1994
Tagungsband der Vorträge und Poster (April 1994)
- No. 2 Extremer Nordsommer '92
Meteorologische Ausprägung, Wirkungen auf naturnahe und vom Menschen beeinflußte Ökosysteme, gesellschaftliche Perzeption und situationsbezogene politisch-administrative bzw. individuelle Maßnahmen (Vol. 1 - Vol. 4)
H.-J. Schellnhuber, W. Enke, M. Flechsig (Mai 1994)
- No. 3 Using Plant Functional Types in a Global Vegetation Model
W. Cramer (September 1994)
- No. 4 Interannual variability of Central European climate parameters and their relation to the large-scale circulation
P. C. Werner (Oktober 1994)
- No. 5 Coupling Global Models of Vegetation Structure and Ecosystem Processes - An Example from Arctic and Boreal Ecosystems
M. Plöchl, W. Cramer (Oktober 1994)
- No. 6 The use of a European forest model in North America: A study of ecosystem response to climate gradients
H. Bugmann, A. Solomon (Mai 1995)
- No. 7 A comparison of forest gap models: Model structure and behaviour
H. Bugmann, Y. Xiaodong, M. T. Sykes, Ph. Martin, M. Lindner, P. V. Desanker, S. G. Cumming (Mai 1995)
- No. 8 Simulating forest dynamics in complex topography using gridded climatic data
H. Bugmann, A. Fischlin (Mai 1995)
- No. 9 Application of two forest succession models at sites in Northeast Germany
P. Lasch, M. Lindner (Juni 1995)
- No. 10 Application of a forest succession model to a continentality gradient through Central Europe
M. Lindner, P. Lasch, W. Cramer (Juni 1995)
- No. 11 Possible Impacts of global warming on tundra and boreal forest ecosystems - Comparison of some biogeochemical models
M. Plöchl, W. Cramer (Juni 1995)
- No. 12 Wirkung von Klimaveränderungen auf Waldökosysteme
P. Lasch, M. Lindner (August 1995)
- No. 13 MOSES - Modellierung und Simulation ökologischer Systeme - Eine Sprachbeschreibung mit Anwendungsbeispielen
V. Wenzel, M. Kücken, M. Flechsig (Dezember 1995)
- No. 14 TOYS - Materials to the Brandenburg biosphere model / GAIA
Part 1 - Simple models of the "Climate + Biosphere" system
Yu. Svirzhev (ed.), A. Block, W. v. Bloh, V. Brovkin, A. Ganopolski, V. Petoukhov, V. Razzhevaikin (Januar 1996)
- No. 15 Änderung von Hochwassercharakteristiken im Zusammenhang mit Klimaänderungen - Stand der Forschung
A. Bronstert (April 1996)
- No. 16 Entwicklung eines Instruments zur Unterstützung der klimapolitischen Entscheidungsfindung
M. Leimbach (Mai 1996)
- No. 17 Hochwasser in Deutschland unter Aspekten globaler Veränderungen - Bericht über das DFG-Rundgespräch am 9. Oktober 1995 in Potsdam
A. Bronstert (ed.) (Juni 1996)
- No. 18 Integrated modelling of hydrology and water quality in mesoscale watersheds
V. Krysanova, D.-I. Müller-Wohlfel, A. Becker (Juli 1996)
- No. 19 Identification of vulnerable subregions in the Elbe drainage basin under global change impact
V. Krysanova, D.-I. Müller-Wohlfel, W. Cramer, A. Becker (Juli 1996)
- No. 20 Simulation of soil moisture patterns using a topography-based model at different scales
D.-I. Müller-Wohlfel, W. Lahmer, W. Cramer, V. Krysanova (Juli 1996)
- No. 21 International relations and global climate change
D. Sprinz, U. Luterbacher (1st ed. July, 2n ed. December 1996)
- No. 22 Modelling the possible impact of climate change on broad-scale vegetation structure - examples from Northern Europe
W. Cramer (August 1996)

- No. 23 A methode to estimate the statistical security for cluster separation
F.-W. Gerstengarbe, P.C. Werner (Oktober 1996)
- No. 24 Improving the behaviour of forest gap models along drought gradients
H. Bugmann, W. Cramer (Januar 1997)
- No. 25 The development of climate scenarios
P.C. Werner, F.-W. Gerstengarbe (Januar 1997)
- No. 26 On the Influence of Southern Hemisphere Winds on North Atlantic Deep Water Flow
S. Rahmstorf, M. H. England (Januar 1977)
- No. 27 Integrated systems analysis at PIK: A brief epistemology
A. Bronstert, V. Brovkin, M. Krol, M. Lüdeke, G. Petschel-Held, Yu. Svirezhev, V. Wenzel (März 1997)
- No. 28 Implementing carbon mitigation measures in the forestry sector - A review
M. Lindner (Mai 1997)
- No. 29 Implementation of a Parallel Version of a Regional Climate Model
M. Kücken, U. Schättler (Oktober 1997)
- No. 30 Comparing global models of terrestrial net primary productivity (NPP): Overview and key results
W. Cramer, D. W. Kicklighter, A. Bondeau, B. Moore III, G. Churkina, A. Ruimy, A. Schloss, participants of "Potsdam '95" (Oktober 1997)
- No. 31 Comparing global models of terrestrial net primary productivity (NPP): Analysis of the seasonal behaviour of NPP, LAI, FPAR along climatic gradients across ecotones
A. Bondeau, J. Kaduk, D. W. Kicklighter, participants of "Potsdam '95" (Oktober 1997)
- No. 32 Evaluation of the physiologically-based forest growth model FORSANA
R. Grote, M. Erhard, F. Suckow (November 1997)
- No. 33 Modelling the Global Carbon Cycle for the Past and Future Evolution of the Earth System
S. Franck, K. Kossacki, Ch. Bounama (Dezember 1997)
- No. 34 Simulation of the global bio-geophysical interactions during the Last Glacial Maximum
C. Kubatzki, M. Claussen (Januar 1998)
- No. 35 CLIMBER-2: A climate system model of intermediate complexity. Part I: Model description and performance for present climate
V. Petoukhov, A. Ganopolski, V. Brovkin, M. Claussen, A. Eliseev, C. Kubatzki, S. Rahmstorf (Februar 1998)
- No. 36 Geocybernetics: Controlling a rather complex dynamical system under uncertainty
H.-J. Schellnhuber, J. Kropp (Februar 1998)
- No. 37 Untersuchung der Auswirkungen erhöhter atmosphärischer CO₂-Konzentrationen auf Weizenbestände des Free-Air Carbon dioxide Enrichment (FACE) - Experimentes Maricopa (USA)
Th. Kartschall, S. Grossman, P. Michaelis, F. Wechsung, J. Gräfe, K. Waloszczyk, G. Wechsung, E. Blum, M. Blum (Februar 1998)
- No. 38 Die Berücksichtigung natürlicher Störungen in der Vegetationsdynamik verschiedener Klimagebiete
K. Thonicke (Februar 1998)
- No. 39 Decadal Variability of the Thermohaline Ocean Circulation
S. Rahmstorf (März 1998)
- No. 40 SANA-Project results and PIK contributions
K. Bellmann, M. Erhard, M. Flechsig, R. Grote, F. Suckow (März 1998)
- No. 41 Umwelt und Sicherheit: Die Rolle von Umweltschwellenwerten in der empirisch-quantitativen Modellierung
D. F. Sprinz (März 1998)
- No. 42 Reversing Course: Germany's Response to the Challenge of Transboundary Air Pollution
D. F. Sprinz, A. Wahl (März 1998)
- No. 43 Modellierung des Wasser- und Stofftransports in großen Einzugsgebieten. Zusammenstellung der Beiträge des Workshops am 15. Dezember 1997 in Potsdam
A. Bronstert, V. Krysanova, A. Schröder, A. Becker, H.-R. Bork (eds.) (April 1998)
- No. 44 Capabilities and Limitations of Physically Based Hydrological Modelling on the Hillslope Scale
A. Bronstert (April 1998)
- No. 45 Sensitivity Analysis of a Forest Gap Model Concerning Current and Future Climate Variability
P. Lasch, F. Suckow, G. Bürger, M. Lindner (Juli 1998)
- No. 46 Wirkung von Klimaveränderungen in mitteleuropäischen Wirtschaftswäldern
M. Lindner (Juli 1998)
- No. 47 SPRINT-S: A Parallelization Tool for Experiments with Simulation Models
M. Flechsig (Juli 1998)

- No. 48 The Odra/Oder Flood in Summer 1997: Proceedings of the European Expert Meeting in Potsdam, 18 May 1998
A. Bronstert, A. Ghazi, J. Hladny, Z. Kundzewicz, L. Menzel (eds.) (September 1998)
- No. 49 Struktur, Aufbau und statistische Programmbibliothek der meteorologischen Datenbank am Potsdam-Institut für Klimafolgenforschung
H. Österle, J. Glauer, M. Denhard (Januar 1999)
- No. 50 The complete non-hierarchical cluster analysis
F.-W. Gerstengarbe, P. C. Werner (Januar 1999)
- No. 51 Struktur der Amplitudengleichung des Klimas
A. Hauschild (April 1999)
- No. 52 Measuring the Effectiveness of International Environmental Regimes
C. Helm, D. F. Sprinz (Mai 1999)
- No. 53 Untersuchung der Auswirkungen erhöhter atmosphärischer CO₂-Konzentrationen innerhalb des Free-Air Carbon Dioxide Enrichment-Experimentes: Ableitung allgemeiner Modelllösungen
Th. Kartschall, J. Gräfe, P. Michaelis, K. Waloszczyk, S. Grossman-Clarke (Juni 1999)
- No. 54 Flächenhafte Modellierung der Evapotranspiration mit TRAIN
L. Menzel (August 1999)
- No. 55 Dry atmosphere asymptotics
N. Botta, R. Klein, A. Almgren (September 1999)
- No. 56 Wachstum von Kiefern-Ökosystemen in Abhängigkeit von Klima und Stoffeintrag - Eine regionale Fallstudie auf Landschaftsebene
M. Erhard (Dezember 1999)
- No. 57 Response of a River Catchment to Climatic Change: Application of Expanded Downscaling to Northern Germany
D.-I. Müller-Wohlfel, G. Bürger, W. Lahmer (Januar 2000)
- No. 58 Der "Index of Sustainable Economic Welfare" und die Neuen Bundesländer in der Übergangsphase
V. Wenzel, N. Herrmann (Februar 2000)
- No. 59 Weather Impacts on Natural, Social and Economic Systems (WISE, ENV4-CT97-0448)
German report
M. Flechsig, K. Gerlinger, N. Herrmann, R. J. T. Klein, M. Schneider, H. Sterr, H.-J. Schellnhuber (Mai 2000)
- No. 60 The Need for De-Aliasing in a Chebyshev Pseudo-Spectral Method
M. Uhlmann (Juni 2000)
- No. 61 National and Regional Climate Change Impact Assessments in the Forestry Sector - Workshop Summary and Abstracts of Oral and Poster Presentations
M. Lindner (ed.) (Juli 2000)
- No. 62 Bewertung ausgewählter Waldfunktionen unter Klimaänderung in Brandenburg
A. Wenzel (August 2000)
- No. 63 Eine Methode zur Validierung von Klimamodellen für die Klimawirkungsforschung hinsichtlich der Wiedergabe extremer Ereignisse
U. Böhm (September 2000)
- No. 64 Die Wirkung von erhöhten atmosphärischen CO₂-Konzentrationen auf die Transpiration eines Weizenbestandes unter Berücksichtigung von Wasser- und Stickstofflimitierung
S. Grossman-Clarke (September 2000)
- No. 65 European Conference on Advances in Flood Research, Proceedings, (Vol. 1 - Vol. 2)
A. Bronstert, Ch. Bismuth, L. Menzel (eds.) (November 2000)
- No. 66 The Rising Tide of Green Unilateralism in World Trade Law - Options for Reconciling the Emerging North-South Conflict
F. Biermann (Dezember 2000)
- No. 67 Coupling Distributed Fortran Applications Using C++ Wrappers and the CORBA Sequence Type
Th. Slawig (Dezember 2000)
- No. 68 A Parallel Algorithm for the Discrete Orthogonal Wavelet Transform
M. Uhlmann (Dezember 2000)
- No. 69 SWIM (Soil and Water Integrated Model), User Manual
V. Krysanova, F. Wechsung, J. Arnold, R. Srinivasan, J. Williams (Dezember 2000)
- No. 70 Stakeholder Successes in Global Environmental Management, Report of Workshop, Potsdam, 8 December 2000
M. Welp (ed.) (April 2001)

- No. 71 GIS-gestützte Analyse globaler Muster anthropogener Waldschädigung - Eine sektorale Anwendung des Syndromkonzepts
M. Cassel-Gintz (Juni 2001)
- No. 72 Wavelets Based on Legendre Polynomials
J. Fröhlich, M. Uhlmann (Juli 2001)